2019-12

MODELING OF MORPHOLOGICAL RESPONSES TO A STORM EVENT DURING TREX13

Santos Pessanha, Vinicius

Monterey, CA; Naval Postgraduate School

NAVAL POSTGRADUATE SCHOOL

MONTEREY, CALIFORNIA

THESIS

MODELING OF MORPHOLOGICAL RESPONSES TO A STORM EVENT DURING TREX13

by

Vinicius Santos Pessanha

December 2019

Thesis Advisor:	Peter C. Chu
Second Reader:	Chenwu Fan (contractor)

THIS PAGE INTENTIONALLY LEFT BLANK

REPORT DOCUMENTATION PAGE			*Form Approved OMB No. 0704-0188*

1. AGENCY USE ONLY *(Leave blank)*	**2. REPORT DATE** December 2019	**3. REPORT TYPE AND DATES COVERED** Master's thesis

4. TITLE AND SUBTITLE MODELING OF MORPHOLOGICAL RESPONSES TO A STORM EVENT DURING TREX13	**5. FUNDING NUMBERS**
6. AUTHOR(S) Vinicius Santos Pessanha	
7. PERFORMING ORGANIZATION NAME(S) AND ADDRESS(ES) Naval Postgraduate School Monterey, CA 93943-5000	**8. PERFORMING ORGANIZATION REPORT NUMBER**
9. SPONSORING / MONITORING AGENCY NAME(S) AND ADDRESS(ES) SERDP, Alexandria, VA 22350	**10. SPONSORING / MONITORING AGENCY REPORT NUMBER**

11. SUPPLEMENTARY NOTES The views expressed in this thesis are those of the author and do not reflect the official policy or position of the Department of Defense or the U.S. Government.

12a. DISTRIBUTION / AVAILABILITY STATEMENT Approved for public release. Distribution is unlimited.	**12b. DISTRIBUTION CODE** A

13. ABSTRACT (maximum 200 words)

Munitions in the underwater environment might be harmful to marine life and human health when their chemical constituents are released into the ocean. A reliable model to appropriately forecast munition location and burial depth can improve risk assessment and reduce costs related to munition remediation actions. Munition mobility and burial models exist to determine the location and burial depth, but they require localized parameters, such as waves and currents. Up to now, nearshore process models to compute these parameters have not been tested for fidelity against observable storm-event experiment results, including munition mobility and near-seabed hydrodynamics, and sediment transport. This study presents an environment hindcasting model for coastal seafloor hydrodynamic and morphologic conditions in a non-muddy seabed using Delft3D software. The model output is compared with measurements made on the coast of Panama City, Florida, during the TREX13 experiment in 2013. The objective is to model the morphological responses to a storm event that occurred in the middle of the experiment period. The results suggest that the model can adequately simulate the flow and the bottom changes measured during the TREX13 experiment, which includes significant wave energy and the accretion of sediment of approximately 15 cm in 24 hours.

14. SUBJECT TERMS munition mobility, burial, Delft3D model, non-muddy seabed	**15. NUMBER OF PAGES** 73
	16. PRICE CODE

17. SECURITY CLASSIFICATION OF REPORT	**18. SECURITY CLASSIFICATION OF THIS PAGE**	**19. SECURITY CLASSIFICATION OF ABSTRACT**	**20. LIMITATION OF ABSTRACT**
Unclassified	Unclassified	Unclassified	UU

NSN 7540-01-280-5500 Standard Form 298 (Rev. 2-89) Prescribed by ANSI Std. 239-18

THIS PAGE INTENTIONALLY LEFT BLANK

Approved for public release. Distribution is unlimited.

MODELING OF MORPHOLOGICAL RESPONSES TO A STORM EVENT DURING TREX13

Vinicius Santos Pessanha
Lieutenant Commander, Brazilian Navy
BS, Brazilian Naval Academy, 2007

Submitted in partial fulfillment of the
requirements for the degree of

MASTER OF SCIENCE IN METEOROLOGY AND PHYSICAL OCEANOGRAPHY

from the

NAVAL POSTGRADUATE SCHOOL
December 2019

Approved by: Peter C. Chu
Advisor

Chenwu Fan
Second Reader

Peter C. Chu
Chair, Department of Oceanography

THIS PAGE INTENTIONALLY LEFT BLANK

ABSTRACT

Munitions in the underwater environment might be harmful to marine life and human health when their chemical constituents are released into the ocean. A reliable model to appropriately forecast munition location and burial depth can improve risk assessment and reduce costs related to munition remediation actions. Munition mobility and burial models exist to determine the location and burial depth, but they require localized parameters, such as waves and currents. Up to now, nearshore process models to compute these parameters have not been tested for fidelity against observable storm-event experiment results, including munition mobility and near-seabed hydrodynamics, and sediment transport. This study presents an environment hindcasting model for coastal seafloor hydrodynamic and morphologic conditions in a non-muddy seabed using Delft3D software. The model output is compared with measurements made on the coast of Panama City, Florida, during the TREX13 experiment in 2013. The objective is to model the morphological responses to a storm event that occurred in the middle of the experiment period. The results suggest that the model can adequately simulate the flow and the bottom changes measured during the TREX13 experiment, which includes significant wave energy and the accretion of sediment of approximately 15 cm in 24 hours.

THIS PAGE INTENTIONALLY LEFT BLANK

TABLE OF CONTENTS

LIST OF FIGURES

LIST OF TABLES

THIS PAGE INTENTIONALLY LEFT BLANK

LIST OF ACRONYMS AND ABBREVIATIONS

3D	three-dimensional
DDB Delft	Delft3D dashboard
Delft3D-Flow	flow module of Delft3D
Delft3D-MOR	morphology module of Delft3D
Delft3D-Wave	wave module of Delft3D
ECMWF	European Centre for Medium-Range Weather Forecasts
JONSWAP	Joint North Sea Wave Project
NDBC	National Data Buoy Center
NGDC	National Geophysical Data Center
NOAA	National Oceanic and Atmospheric Administration
SERDP	Strategic Environmental Research and Development Program
SWAN	Simulating Waves Nearshore
TREX13	Target Reverberation Experiment 2013

THIS PAGE INTENTIONALLY LEFT BLANK

ACKNOWLEDGMENTS

This thesis is dedicated to my wife, Thiciane, and son, Pedro. Their support and love were essential in overcoming all difficulties. I love you.

First, I would like to express my feelings of gratitude to Dr. Peter C. Chu for all the assistance, kindness, dedication, and valuable insights. Professor Chu, thank you very much! Second, my thanks go to the Brazilian Navy for giving me the opportunity to study at such a prestigious institution. Third, I would like to express my appreciation to Professor Mara Orescanin for the productive discussions about wave modeling, Dr. Joseph Calantoni for providing the TREX13 experiment data, and Mike Cook for the many times he answered my MATLAB questions. I also have to mention Mr. Chenwu Fan for assistance with this thesis. My parents, Nelson and Lucia, and my brothers, Welington and Bruno, deserve my special gratitude for their encouragement and unconditional love.

Lastly, I give sincere thanks to the faculty and staff of the Department of Oceanography and the Department of Meteorology, my classmates, and others who helped me along the way.

THIS PAGE INTENTIONALLY LEFT BLANK

I. INTRODUCTION

A. CONTEXT

According to Strategic Environmental Research and Development Program (SERDP 2010), the U.S. Army Corps of Engineers, Navy, and Marine Corps have identified more than 430 locations in the United States (Figure 1) as potentially containing underwater munitions. They took into account the location of former military bases and records of shipwrecks, ocean disposal operations, accidents, and training areas. The release of chemical elements from munitions might be harmful to marine life and to human health, which highlights the importance of well-organized actions to mitigate this problem. Thus, an efficient model to forecast the location and burial depth of such munitions can improve risk assessment and reduce costs related to remediation actions.

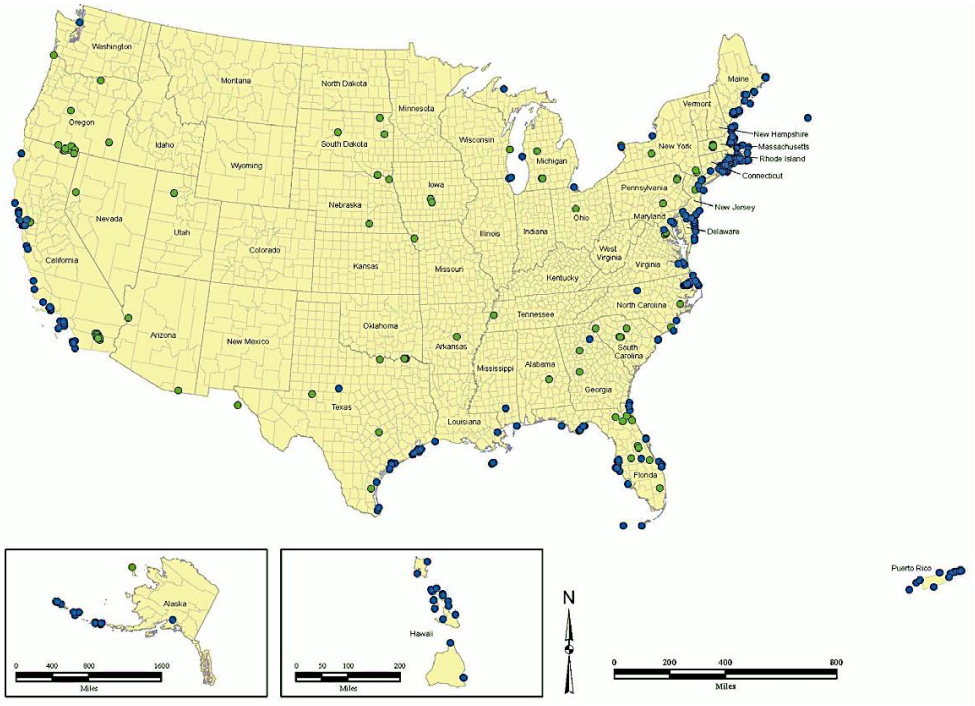

The green dots represent inland waters, and the blue ones represent tidal waters.

Figure 1. Sites potentially containing munitions in underwater environments. Source: MacDonald (2009).

Models exist to determine the location and burial depth on muddy and sandy seabeds in nearshore environments, which can present reliable results in modeling underwater munitions. A good example is the impact burial model (IMPACT35), which was developed to forecast the burial upon impact on a muddy bed (Chu and Fan 2006). Also, the unexploded ordnance impact mobility model Vortex-Lattice simulates burial of munitions on a sandy bed (Jenkins et al. 2007). These models require localized environmental parameters such as waves and currents, however, in order to accurately predict the location, mobility, and burial state of underwater munitions.

Up to now, nearshore models to compute these parameters have not been thoroughly tested against observable storm-event experiment results including both munition mobility and near-seabed hydrodynamics and sediment transport. The purpose of this study is to test the ability of the Delft3D nearshore processes model to simulate the hydrodynamic and morphological processes during strong storm events that are capable of moving heavy munitions in a sandy seafloor. This research utilizes data from the Target Reverberation Experiment 2013 (TREX13) in Panama City, Florida, to asses this modeling system. The TREX13 experiment produced a unique data set containing measurements such as waves and currents and also mobility and burial of munitions (Calantoni 2014).

The ability to remove a munition depends upon the location of the munition and its burial depth. The location can be affected by mobility caused by currents and waves. Burial, in a sandy bed, is affected by the scour due to currents and sediment transport. Morphodynamics of the nearshore environment comprise several processes. Waves, currents, and sediment transport are the most critical processes that lead to seafloor change. Moreover, variation in these environment features may cause burial and mobility of submerged munitions. When wind transmits momentum to the water surface, it may form waves that produce near-seabed orbital motion responsible for stirred-up sediment, increasing the sediment transport. In contrast, wave orbital motion in the company of currents intensifies the bed shear stress, decreasing the intensity of the current. Furthermore, the dissipation of wave energy in the surf zone induces currents along and across the shore (Roelvink and Reniers 2012). All these littoral flows carry a significant

quantity of sediments (Komar 1976). Predicting a munition's burial and mobility is a challenge considering all the processes involved in this.

The open source software Delft3D is capable of modeling littoral flows, waves, sediment transport, and morphological changes in the nearshore area (Deltares 2019a). Model output from Delft3D provides the neighboring environment required parameters to the munition's models such as IMPACT35 and Vortex-Lattice to predict a munition's burial and mobility.

B. OBJECTIVE

This study presents an environment hindcasting model for coastal seafloor hydrodynamic and morphologic conditions in a non-muddy seabed using Delft3D software. The model output is compared with measurements made on the coast of Panama City, Florida. The objective is modeling the morphological responses to storm events during the TREX13 experiment. The performance evaluation of the environmental model will contribute to a future coupling of this model with the Vortex-Lattice model.

C. ORGANIZATION

Chapter II presents the study area. It also explains the TREX13 experiment and describes the flow, wave, and transport modules of the Delft3D model presenting the main equations. Chapter III details the model setup, computational grids, boundary conditions, and parameter settings. Chapter IV shows the model calibration for water level, wave and current. Chapter V examines the results of the model. Chapter VI discusses the conclusions.

THIS PAGE INTENTIONALLY LEFT BLANK

II. BACKGROUND

This study used data from the TREX13 to calibrate and validate the Delft3D model. This chapter describes the field site and summarizes the paper from Calantoni (2014). It also describes the Delft3D modeling system based on the user manual from Deltares (2019a). The objective of this chapter is to provide an overview of the foundational research that this study builds upon and to present the governing equations of the Delft3D model.

A. FIELD SITE

1. Location

The study area, within the northern Gulf of Mexico, is on the coast of Panama City, Florida (Figure 2). Chapter III Section C describes in more detail the extension of the model domain.

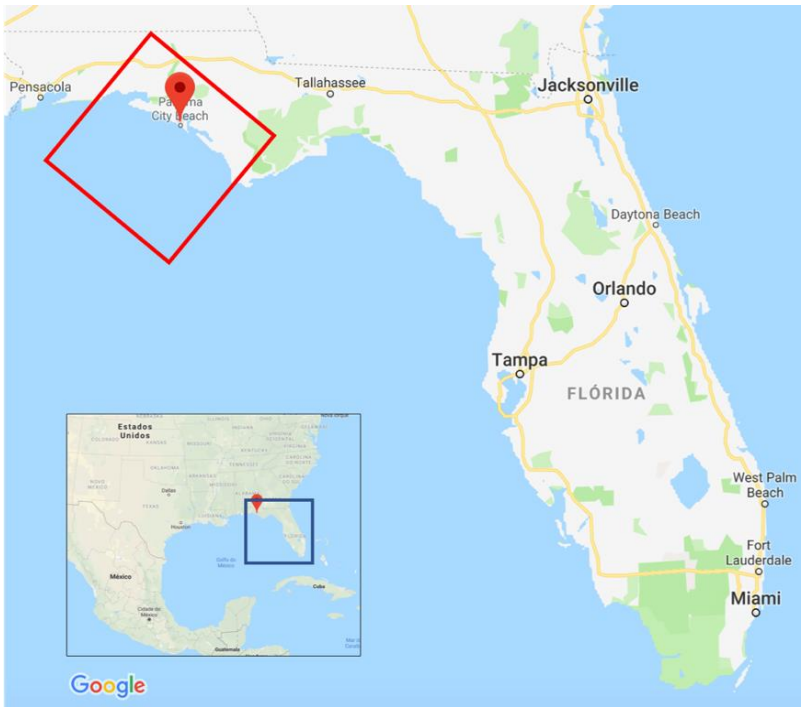

The location of the study area is highlighted by the red rectangle.

Figure 2. Study area. Adapted from Google Maps (2019).

2. Hydrodynamical Forcing

Tide, wind, and waves are the main hydrodynamical forcing in the study area.

a. Tide

The area off the coast of Panama City has a diurnally dominated tide, which means it experiences one high tide and one low tide each lunar day. According to Bunya et al. (2010), the main tide components have amplitudes varying less than 0.4 m in the area of interest.

b. Wind and Waves

According to Chu et al. (2006), the wind in the northern Gulf of Mexico follows a seasonal pattern. In winter and fall, winds are primarily from the north. In contrast, winds come mostly from the south in summer and spring. The mean wind intensity is weak, generally around 3 m/s. Panama City is usually a low-energetic location (Calantoni 2014), where the mean wave period is 8 seconds and the mean wave height is 0.9 m (Farrar et al. 1994). In the hurricane season, from June to November, the high waves and surge associated with sporadic storms can cause significant morphologic changes on the coast of Panama City (Taiani et al. 2012).

c. Seabed Sediment

In the area of study, the sedimentation is primarily quartz sand with a density of approximately 2,650 kg/m^3 (Plant et al. 2013). The mean size of sediment collected during TREX13 is around $\varphi = 2.1$ (Calantoni 2014).

B. FIELD EXPERIMENT

1. TREX13

According to Calantoni (2014), during the field experiment TREX13 that occurred on the coast of Panama City, Florida, in April and May 2013, surrogate munitions of different sizes and density (fabricated from distinctive types of metal) were placed on the seafloor and had their location recorded continuously. At the same time, instruments measured environment features such as the wave direction and height, currents, and

sediment transport at high temporal and spatial resolution. The objective was to accurately measure the processes causing burial, scour, and movement of munitions on the seabed.

The surrogate munitions were designed to simulate real munitions but did not have an explosive component. Figure 3 shows the munitions used in the experiment.

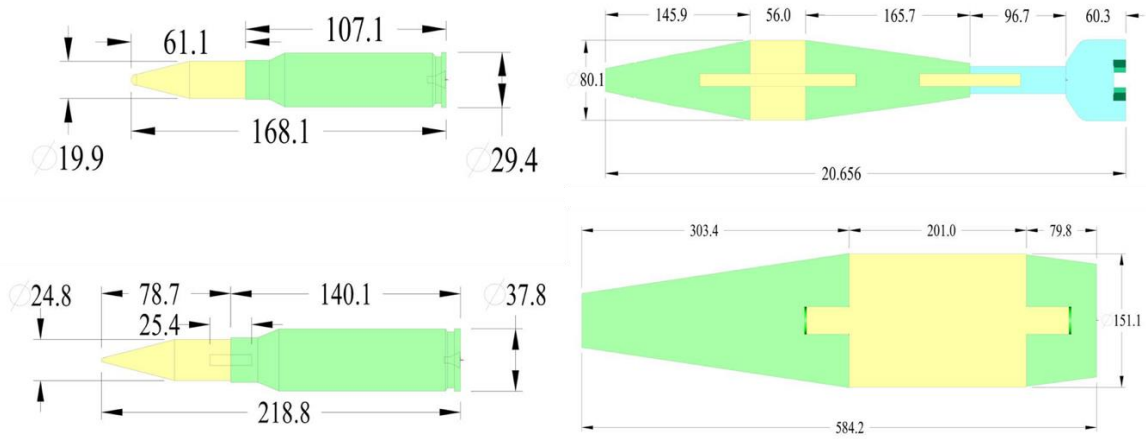

Surrogate munitions were designed for 20mm cartridge (top left), 25mm cartridge (bottom left), 81mm mortar (top right), and 155mm, HE, M107 (bottom right).

Figure 3. Surrogate munitions of different sizes used in the experiment. Adapted from Calantoni (2014).

Two metal structures called “quadpods” (Figure 4) were used to install the instruments, such as sonar scanners and pencil-beam sector scanners, acoustic Doppler current profilers, and pulse coherent acoustic Doppler profilers. Both quadpods were deployed on April 20, and divers laid the surrogate munitions of different sizes under each quadpod following a predetermined scheme. The quadpods were arranged cross-shore (Figure 4), one at the depth of 7.5m (shallow quadpod), and another at the depth of 20m (deep quadpod). All equipment was retrieved on May 23, 2013.

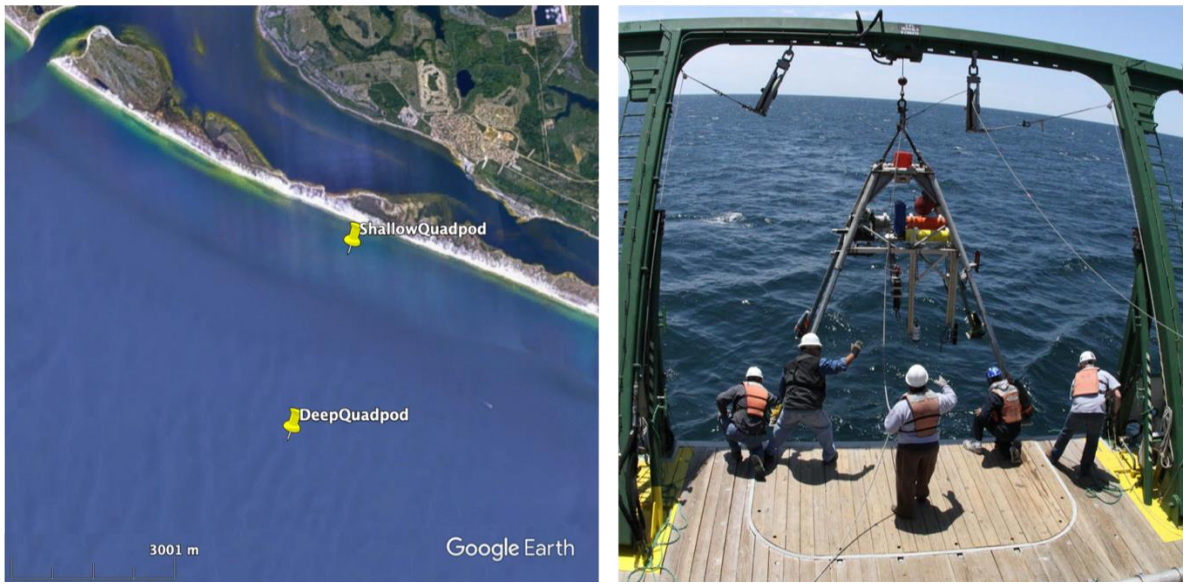

On the left, the location of the shallow quadpod at 30° 04.81 N, 85° 40.41 W, and the location of the deep quadpod at 30° 03.02 N, 85° 41.34 W. On the right, is a picture of the deep quadpod's deployment.

Figure 4. Quadpod location and deployment. Adapted from Google Earth (2019) and Calantoni (2014).

2. The Storm Event

The most interesting period of observation occurred between May 5 and 6, when a storm event caused large waves, munition mobility, and seabed changes. During the storm, equipment measured wave height at more than 2 meters and wave peak period at approximately 7 seconds. At the shallow quadpod's location, a quick burial of all munitions (Figure 5) and a significant accretion of sediment (approximately 0.15 meters of sand) was observed. In contrast, at the deep quadpod's location, no munition mobility or seabed change was detected.

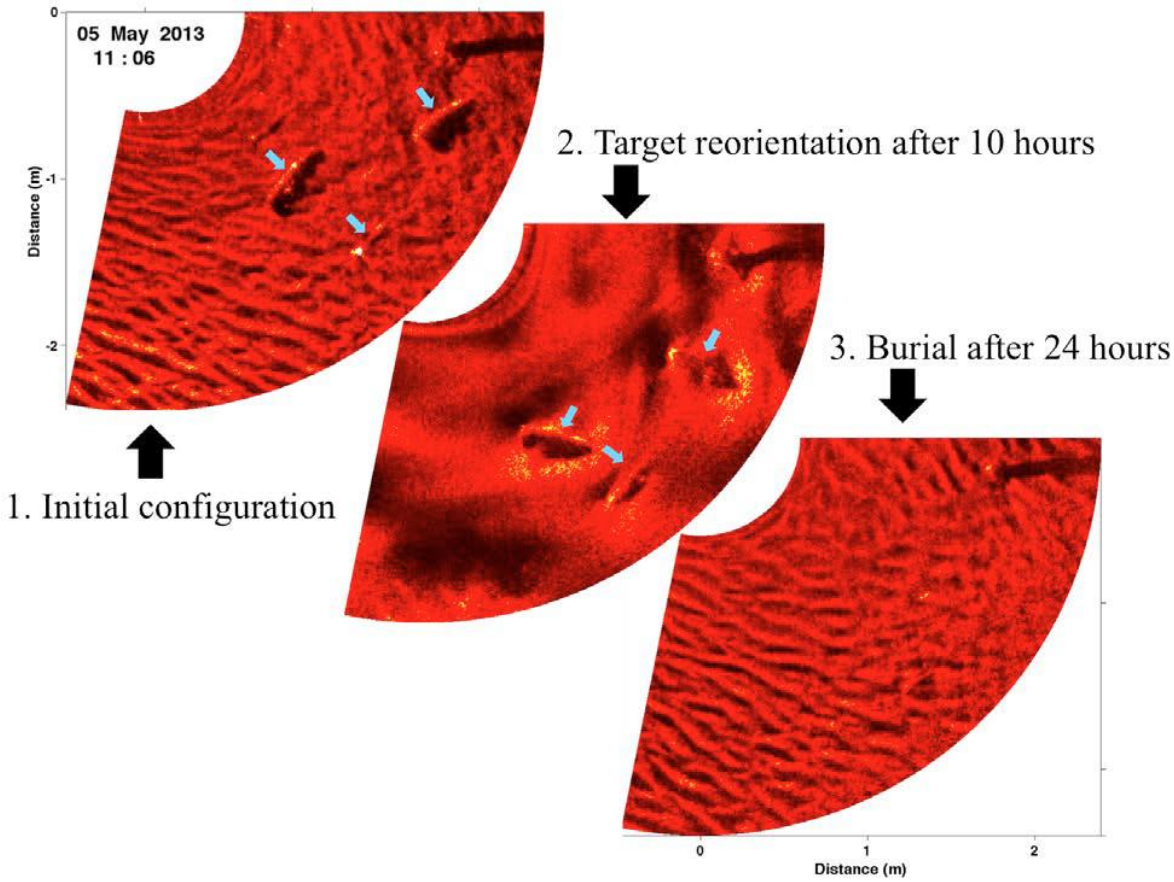

This figure shows a sequence of sector-scanning sonar images of the shallow quadpod's location displaying the munition burial and mobility during the storm event. Blue arrows show the munition's position. Total burial occurs after 24 hours.

Figure 5. Munition burial and mobility during the storm event. Source: Calantoni (2014).

More about the TREX13 results is discussed in Chapter IV.

C. MODEL DESCRIPTION

Delft3D is an open-source modeling system that incorporates many integrated modules for different nearshore simulation purposes. This section provides a description of the flow, wave, and transport modules.

1. Flow Module

The flow module Delft3D-Flow is responsible for feeding the hydrodynamic input to the wave and transport modules. It can model two-dimensional or three-dimensional

(3D) non-steady flow forced by tides and winds, solving shallow water equations. Also, it can account for density-driven flow (Deltares 2019a).

a. Horizontal Coordinate System

Delft3D uses orthogonal curvilinear coordinates in the horizontal direction. The model supports both Cartesian (ξ,η) and spherical (λ,ϕ) coordinates, considering the spherical coordinates as a particular occurrence of orthogonal curvilinear coordinates, where: $\xi=\lambda$, $\eta=\phi$, $\sqrt{G_{\xi\xi}}=R\cos\phi$, and $\sqrt{G_{\eta\eta}}=R$. Here, ξ and η are horizontal curvilinear coordinates, λ represents longitude, ϕ is latitude, $\sqrt{G_{\xi\xi}}$ and $\sqrt{G_{\eta\eta}}$ are an artifice to convert curvilinear to rectangular coordinates, and R is the radius of the Earth.

b. Vertical Coordinate System

Both σ and z vertical coordinate systems are available in the flow module. According to Phillips (1957), the σ coordinate system was initially developed for atmospheric models. In this system, the vertical grid contains layers limited by two σ-planes that smoothly follow the bottom shape, with $\sigma=z-\zeta/H$, where z is the vertical coordinate from mean surface level, ζ is the water level, and H is the total depth (depth + water level). The quantity of layers is the same over the whole domain, and the layer thickness is usually variable to allow better resolution in the areas of concern. Furthermore, the surface and the bottom of the seabed are represented as coordinate lines, $\sigma=0$ and $\sigma=-1$, respectively (Figure 6).

In the z coordinate system, each layer is bounded by two parallel planes that follow the isopycnals in steep bottom slope areas. In addition, the bottom is pictured as a zigzag boundary, and the free surface and bottom of the seabed are typically not considered as a coordinate line (Figure 6).

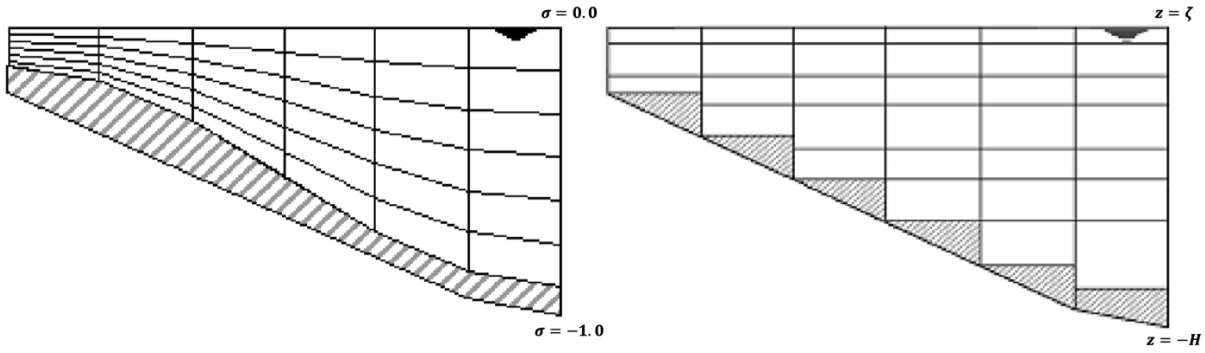

This figure presents the vertical coordinate system σ, on the left, and z, on the right. Here, ζ is the water level and H is the total depth (depth + water level).

Figure 6. Vertical coordinate systems. Source: Deltares (2019a).

c. System of Equations

Transport, continuity, and horizontal equations of motion deduced from the Navier–Stokes equations for incompressible flow make up the system of equations. Delft3D-Flow adopts a shallow water approximation, which simplifies the vertical momentum equation into the hydrostatic pressure equation. The Delft3d-Flow equations presented in this chapter refer to horizontal orthogonal curvilinear and vertical σ coordinate systems.

(1) Continuity Equation

The integration of the continuity equation for incompressible fluids over depth gives origin to the depth-averaged continuity equation, which is

$$\frac{\partial \zeta}{\partial t} + \frac{1}{\sqrt{G_{\xi\xi}}\sqrt{G_{\eta\eta}}} \frac{\partial \left((d+\zeta) U \sqrt{G_{\eta\eta}} \right)}{\partial \xi} + \frac{1}{\sqrt{G_{\xi\xi}}\sqrt{G_{\eta\eta}}} \frac{\partial \left((d+\zeta) V \sqrt{G_{\xi\xi}} \right)}{\partial \eta} = (d+\zeta) Q \quad (1)$$

where t is time, d represents depth, ζ is the water level, Q is the total source and sink per unit area, and U and V are barotropic velocities in ξ and η directions, respectively.

(2) Horizontal Equations of Motion

The horizontal momentum equations are

$$\frac{\partial u}{\partial t}+\frac{u}{\sqrt{G_{\xi\xi}}}\frac{\partial u}{\partial \xi}+\frac{v}{\sqrt{G_{\eta\eta}}}\frac{\partial u}{\partial \eta}+\frac{\omega}{d+\zeta}\frac{\partial u}{\partial \sigma}-\frac{v^2}{\sqrt{G_{\xi\xi}}\sqrt{G_{\eta\eta}}}\frac{\partial \sqrt{G_{\eta\eta}}}{\partial \xi}+\frac{uv}{\sqrt{G_{\xi\xi}}\sqrt{G_{\eta\eta}}}\frac{\partial \sqrt{G_{\xi\xi}}}{\partial \eta}+$$
$$-fv=-\frac{1}{\rho_0\sqrt{G_{\xi\xi}}}P_\xi+F_\xi+\frac{1}{(d+\zeta)^2}\frac{\partial}{\partial \sigma}\left(\upsilon_V\frac{\partial u}{\partial \sigma}\right)+M_\xi \tag{2}$$

and

$$\frac{\partial v}{\partial t}+\frac{u}{\sqrt{G_{\xi\xi}}}\frac{\partial v}{\partial \xi}+\frac{v}{\sqrt{G_{\eta\eta}}}\frac{\partial v}{\partial \eta}+\frac{\omega}{d+\zeta}\frac{\partial v}{\partial \sigma}+\frac{uv}{\sqrt{G_{\xi\xi}}\sqrt{G_{\eta\eta}}}\frac{\partial \sqrt{G_{\eta\eta}}}{\partial \xi}-\frac{u^2}{\sqrt{G_{\xi\xi}}\sqrt{G_{\eta\eta}}}\frac{\partial \sqrt{G_{\xi\xi}}}{\partial \eta}+$$
$$+fu=-\frac{1}{\rho_0\sqrt{G_{\eta\eta}}}P_\eta+F_\eta+\frac{1}{(d+\zeta)^2}\frac{\partial}{\partial \sigma}\left(\upsilon_V\frac{\partial v}{\partial \sigma}\right)+M_\eta \tag{3}$$

in which u and v are the velocities in ξ and η directions, respectively, σ signifies vertical coordinate, ω is the velocity in the σ direction, f corresponds to Coriolis parameter, υ_V is the vertical eddy viscosity, ρ_0 is the reference density of water, P_ξ and P_η are gradient hydrostatic pressures, F_ξ and F_η mean turbulent momentum fluxes, and M_ξ and M_η are source and sink of momentum in ξ and η directions, respectively.

(3) Transport Equation

In the flow module, the transport of dissolved substances, heat, and salinity is solved using the equation

$$\frac{\partial (d+\zeta)c}{\partial t}+\frac{1}{\sqrt{G_{\xi\xi}}\sqrt{G_{\eta\eta}}}\left\{\frac{\partial\left[\sqrt{G_{\eta\eta}}(d+\zeta)uc\right]}{\partial \xi}+\frac{\partial\left[\sqrt{G_{\xi\xi}}(d+\zeta)vc\right]}{\partial \eta}\right\}+$$
$$+\frac{\partial \omega c}{\partial \sigma}=\frac{d+\zeta}{\sqrt{G_{\xi\xi}}\sqrt{G_{\eta\eta}}}\left\{\frac{\partial}{\partial \xi}\left(D_H\frac{\sqrt{G_{\eta\eta}}}{\sqrt{G_{\xi\xi}}}\frac{\partial c}{\partial \xi}\right)+\frac{\partial}{\partial \eta}\left(D_H\frac{\sqrt{G_{\xi\xi}}}{\sqrt{G_{\eta\eta}}}\frac{\partial c}{\partial \eta}\right)\right\}+ \tag{4}$$
$$+\frac{1}{d+\zeta}\frac{\partial}{\partial \sigma}\left(D_V\frac{\partial c}{\partial \sigma}\right)-\lambda_d(d+\zeta)c+S$$

where D_H is the horizontal diffusion coefficient, D_V is the vertical diffusion coefficient, λ_d is the first-order decay process (represents an exponentially decreasing numerical solution), and S is the source/sink terms.

(4) Vertical Velocity

The vertical velocity ω is with respect to the σ-plane, which can be understood as the velocity related to upwelling and downwelling motions. It is possible to calculate the vertical velocity using the continuity equation

$$\frac{\partial \zeta}{\partial t}+\frac{1}{\sqrt{G_{\xi\xi}}\sqrt{G_{\eta\eta}}}\frac{\partial\left((d+\zeta)U\sqrt{G_{\eta\eta}}\right)}{\partial \xi}+\frac{1}{\sqrt{G_{\xi\xi}}\sqrt{G_{\eta\eta}}}\frac{\partial\left((d+\zeta)V\sqrt{G_{\xi\xi}}\right)}{\partial \eta}+ \\ +\frac{\partial \omega}{\partial \sigma}=(d+\zeta)(q_{in}-q_{out}) \tag{5}$$

in which q_{in} is the local source and q_{out} is the local sink of water per unit of volume.

2. Wave Module

The Delft3D-Wave module simulates the generation of the wave by the wind. It is also capable of modeling wave propagation and dissipation in the nearshore environment as well as non-linear wave-wave interactions. This computation, however, demands specific inputs such as water level, bathymetry, wind, and current fields, which are provided by Delft3D-Flow (Deltares 2019b). The wave module uses Simulating Waves Nearshore (SWAN), which is a third-generation model derived from a Eulerian wave action balance equation (Booij et al. 1999).

a. Action Balance Equation

Whitham (1974) states that action density spectrum $N(\sigma,\theta)$ is conserved in the company of currents; the same does not happen with energy density spectrum $E(\sigma,\theta)$. This explains why wave models commonly use $N(\sigma,\theta)$ to depict waves. Here, σ and θ

are relative frequency and wave direction, respectively. The action density is related with energy density, as shown by the equation $N(\sigma,\theta) = E(\sigma,\theta)/\sigma$.

Hasselmann et al. (1973) presented the action balance equation in a Eulerian approach

$$\frac{\partial}{\partial t}N + \frac{\partial}{\partial x}c_x N + \frac{\partial}{\partial y}c_y N + \frac{\partial}{\partial \sigma}c_\sigma N + \frac{\partial}{\partial \theta}c_\theta N = \frac{S}{\sigma} \tag{6}$$

where c is wave propagation speed in x, y, σ, and θ space, and S is the source/sink terms.

b. Wind Source Term

The SWAN model uses Miles-Phillips mechanisms to consider the wind's energy transfer to waves. So, wind input is defined as

$$S_{in}(\sigma,\theta) = A + BE(\sigma,\theta) \tag{7}$$

where A represents the sum of linear growth and BE acts as the exponential growth. Deltares (2019b) provides more details on parameters A and B.

c. Nonlinear Wave-Wave Interactions

According to Hasselmann (1962), a quadruplet is a set of four waves that can interact with each other, exchanging energy and creating nonlinearities. Although initially powerless, this interplay can have a protrusive development after travel through a considerable area, rising wave peak. Moreover, Booij et al. (1999) states that in deep water, a quadruplet moves the wave spectral peak's energy to both lower and higher frequencies (causing dissipation by whitecapping). SWAN adopts the Discrete Interaction Approximation of Hasselmann et al. (1985) to describe the quadruplets.

Triad is another kind of nonlinearity that occurs in the shallow water redirecting energy out of lower to higher frequencies that might produce higher harmonics. The SWAN model uses the Lumped Triad Approximation from Eldeberky and Battjes (1996), which is capable of depicting the triad nonlinearity (Booij et al. 1999).

d. Dissipation Term

The dissipation term is the sum of three contributors: whitecapping $S_{ds,w}(\sigma,\theta)$, bottom friction $S_{ds,b}(\sigma,\theta)$, and depth-induced breaking $S_{ds,br}(\sigma,\theta)$. In SWAN, the whitecapping adopts the WAMDI Group (1988) version of the pulse-based model from Hassemann (1974)

$$S_{ds,w}(\sigma,\theta) = -\Gamma\tilde{\sigma}\frac{k}{\tilde{k}}E(\sigma,\theta) \tag{8}$$

in which Γ denotes the steepness factor, k is wave number, $\tilde{\sigma}$ corresponds to mean frequency, and $\tilde{k}$ signifies the mean wave number.

The bottom friction is determined by the equation

$$S_{ds,b}(\sigma,\theta) = -C_{bottom}\frac{\sigma^2}{g^2 sinh^2(kd)}E(\sigma,\theta) \tag{9}$$

where C_{bottom} is the bottom friction coefficient and d is the water depth. In this equation, SWAN considers the Joint North Sea Wave Project (JONSWAP) empirical model from Hasselmann et al. (1973) and the eddy viscosity model of Madsen et al. (1988). It also applies the drag law model from Collins (1972).

The model from Battjes and Janssen (1978) is applied in SWAN to simulate the depth-induced wave breaking, as shown by the equation

$$S_{ds,br}(\sigma,\theta) = -\frac{S_{ds,br,tot}}{E_{tot}}E(\sigma,\theta) \tag{10}$$

in which E_{tot} signifies total wave energy and $S_{ds,br,tot}$ denotes the rate of depth-induced wave breaking dissipation of E_{tot}.

3. Sediment Transport and Morphology Model

In addition to calculating the hydrodynamics, Delft3D-Flow is also able to compute the sediment transport and update the bathymetry. It solves the advection-diffusion

equation and uses an empirical formulation to evaluate the suspended sediment transport and the bedload transport.

Delft3D-MOR works in an integrated way with the wave and flow modules in a cycle. This system is a process-based model that considers the impact of the wave, currents, and sediment transport on morphological changes. Delft3D-Flow and Delft3D-Wave provide the hydrodynamic input to Delft3D-MOR, which updates the bathymetry considering the sediment transport field. In its turn, the bathymetry feeds back to the flow and wave modules, and the loop restarts (Figure 7).

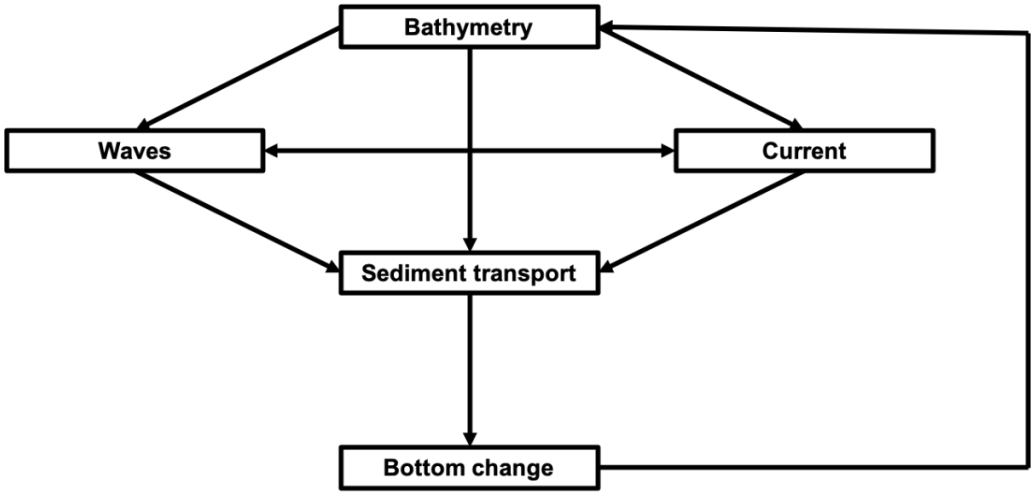

Figure 7. Schematic of the Delft3D-MOR loop. Adapted from Roelvink and Reniers (2012).

a. Sediment Transport

Delft3D supports both cohesive (e.g., silt and clay) and non-cohesive (e.g., gravel and sand) sediments. The transport is classified into two distinct categories: bedload and suspended load transport (Figure 8).

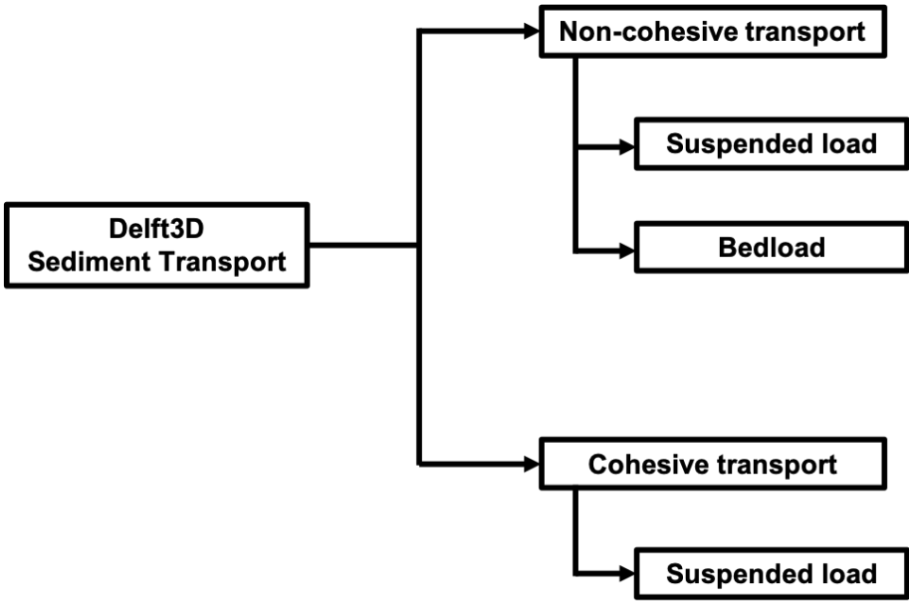

Figure 8. Sediment transport categories in the Delft3D model.

Despite being supported by Delft3D, cohesive transport will not be addressed here, as this work is limited with the sandy seabed.

b. Reference Height

The reference height (a) defines the superior limit of the thin bottom layer with no turbulence effects. It is used to classify suspended and bedload transport in Delft3D. Therefore, bedload transport takes place under the reference height, unlike suspended load transport that occurs above the reference height due to its dependence on turbulence. According to Van Rijn (1993), the reference height can be calculated by:

$$a = min\left[max\left\{ AksFac.k_s, \frac{\Delta_r}{2}, 0.01h \right\}, 0.20h \right] \tag{11}$$

considering $AksFac$ as the proportionality factor (user input), k_s as the current-related effective roughness height (user input), Δ_r as the wave-induced ripple height, and h as the water depth.

c. Bedload Transport

Bedload transport occurs due to saltation and rolling within a slim layer over the seafloor. This kind of transport is directly caused by the energy from the flow. In the bedload theory, the sediment starts to move when the forces promoting movement (e.g., fluid drag and lift force due to pressure gradient) are more significant than the forces hindering movement (e.g., gravity and friction). The kinetic energy transferred from the water to the grain is governed by the fluid's mass and flow velocity. In this context, the critical velocity (u^*) is defined as the flow velocity necessary to move a particle of a particular dimension and density. The critical velocity is essential to compute the critical bed shear stress ($\tau_{b,cr}$), which is used to solve the critical Shields criterion (θ_{cr}) (Shields 1936).

The Shields criterion is used to determine the beginning of sediment motion in a fluid. This parameter defines the greatest grain size (D) that can be moved by a flow velocity u, and it is estimated as

$$\theta_{cr} = \frac{\tau_{b,cr}}{\left[\left(\rho_s - \rho\right) g D_{50}\right]} \tag{12}$$

where ρ_S corresponds to the sediment density, ρ is the water density, g denotes gravity, and D_{50} is the mean diameter of the particle.

Delft3D uses the following estimation method of Van Rijn (2003) to calculate the bedload transport (S_b) as presented in Deltares (2019a)

$$\left|S_b\right| = 0.006 \rho_s \omega_s D_{50}{}^{(l)} M^{0.5} M_e^{0.7} \tag{13}$$

where ω_S is the settling velocity, l denotes the sediment fraction, M is sediment mobility number cause by currents and waves, and M_e is excess sediment mobility number.

The sediment mobility number is derived by the equation

$$M = \frac{v_{eff}^2}{\left(s-1\right) g D_{50}} \tag{14}$$

considering that s is relative density of sediment fraction $\left(\rho_s / \rho\right)$ and υ_{eff} signifies an effective velocity cause by currents and waves.

The excess sediment mobility number can be calculated by the equation

$$M_e = \frac{\left(v_{eff} - v_{cr}\right)^2}{\left(s-1\right) g D_{50}} \tag{15}$$

in which υ_{cr} is critical barotropic velocity for the starting movement (parameter from Shields' theory).

The effective velocity can be computed by the equation

$$v_{eff} = \sqrt{v_R^2 + U_{on}^2} \tag{16}$$

considering that υ_R corresponds to the barotropic velocity calculated from the velocity in the bottom layer and U_{on} is the high frequency near-bed orbital velocities caused by short waves.

d. Suspended Load Transport

Suspended load corresponds to the portion of sediment that is transported above the bedload level. It uses the turbulence kinetic energy to maintain the sediment in the water column. Therefore, the upward turbulent component of velocity needs to be greater than the settling velocity. Hence, this type of sediment transport responds to variations in the flow or wave conditions.

The suspended load transport can be divided into two components: current-related $\left(q_{s,c}\right)$ as a result of the steady flow (average current velocity) and wave-related $\left(S_{s,w}\right)$, which is due to the oscillatory cross-shore orbital motion (Van Rijn 2014). Thus, the total suspended load transport $\left(q_s\right)$ is given by:

$$q_s = q_{s,c} + S_{s,w}\,. \tag{17}$$

Van Rijn (1993) developed an equation to compute the current-related suspended load transport

$$q_{s,c} = \int_a^h uc\,dz \tag{18}$$

where a is reference height, h means water surface, u corresponds to the flow velocity, and c is the sediment concentration.

Delft3D-Flow provides the flow velocity (u). So, in order to obtain the sediment concentration c to calculate $q_{s,c}$, Delft3D-MOR solves the advection-diffusion equation described by:

$$\frac{\partial c^{(l)}}{\partial t} + \frac{\partial uc^{(l)}}{\partial x} + \frac{\partial vc^{(l)}}{\partial y} + \frac{\partial \left(w - w_s^{(l)}\right)c^{(l)}}{\partial z} = \frac{\partial}{\partial x}\left(\varepsilon_{s,x}^{(l)}\frac{\partial c^{(l)}}{\partial x}\right) + \frac{\partial}{\partial y}\left(\varepsilon_{s,y}^{(l)}\frac{\partial c^{(l)}}{\partial y}\right) + \\ + \frac{\partial}{\partial z}\left(\varepsilon_{s,z}^{(l)}\frac{\partial c^{(l)}}{\partial z}\right) + S \tag{19}$$

in which u, v, and w are flow velocities in x, y and z directions respectively, $c^{(l)}$ corresponds to sediment concentration, $w_s^{(l)}$ corresponds to the sediment settling velocity, $\varepsilon_s^{(l)}$ is eddy diffusivity, l is sediment fraction, and S denotes sediment source/sink term.

Van Rijn (2000), based on observations and experiments, also introduced a formula to estimate the wave-related suspended load transport $(S_{s,w})$ as a function of the calibration parameter (f_{SUSW}), phase-lag coefficient (γ=0.2), velocity skewness parameter $\left(U_A\right)$, and suspended sediment load $(L_T = 0.007\rho_s D_{50} M_e)$

$$S_{s,w} = f_{SUSW}\gamma U_A L_T\,. \tag{20}$$

D. SUMMARY

The TREX13 experiment took place on the coast of Panama City, Florida, producing a significant data set. Observations from the storm event occurring between May 5 and 6 showed a rapid burial of the munitions. Additionally, measurements of the boundary layer processes (e.g., wave, currents, and bed change) were made, which provides the necessary records for a modeling study.

The flow, wave, and transport modules of the open-source model Delft3D are described in this chapter. The flow module resolves the shallow water equations in order to provide the hydrodynamic input to wave and transport modules. The wave module uses the SWAN model to simulate the wave generation, propagation, wave-wave interaction, and dissipation by solving the action balance equation. Finally, the transport module calculates the sediment transport by resolving the advection-diffusion equation updating the bathymetry.

THIS PAGE INTENTIONALLY LEFT BLANK

III. MODEL SETUP

Delft3D version 4.04.01 was used to implement a numerical model on the coast of Panama City. This model includes hydrodynamic calculation, wave propagation, sediment transport, and morphological evolution. This chapter presents the model setup applied in this study.

A. DELFT DASHBOARD

Delft Dashboard (DDB) has several features that assist in setting up models. It is based on MATLAB and integrated with Delft3D. It also has access to online databases that can provide bathymetry, tide information, buoy data, and more. In this project, grids were generated and tide-forcing boundary conditions were established in the DDB.

B. TWO-DIMENSIONAL MODEL

The area of interest was considered vertically well mixed; hence, the density stratification was assumed to be insignificant. Thus, the two-dimensional barotropic model approach was adopted.

C. COMPUTATIONAL GRIDS

1. Flow Grids

Two nested rectangular grids compose the flow domain (Figure 9). The flow outer grid (coarser resolution) is large enough to cover the location of the Panama City Beach tide station, and the flow inner grid (finer resolution) includes the location of shallow and deep quadpods used in the TREX13 experiment. Table 1 presents more details about the flow grids.

Table 1. Flow grids details.

Grid Name	Grid Size (km)	M	N	Cell Size (km)
Flow outer	47.2x21	472	210	0.1x0.1
Flow inner	7.5x6	300	240	0.025x0.025

M and N signify number of cells in longshore and cross-shore directions, respectively.

The sediment transport and morphological evolution were computed only in the flow inner grid to allow the comparison with TREX13 experiment measurements. The resolution of the flow inner grid is 25 meters.

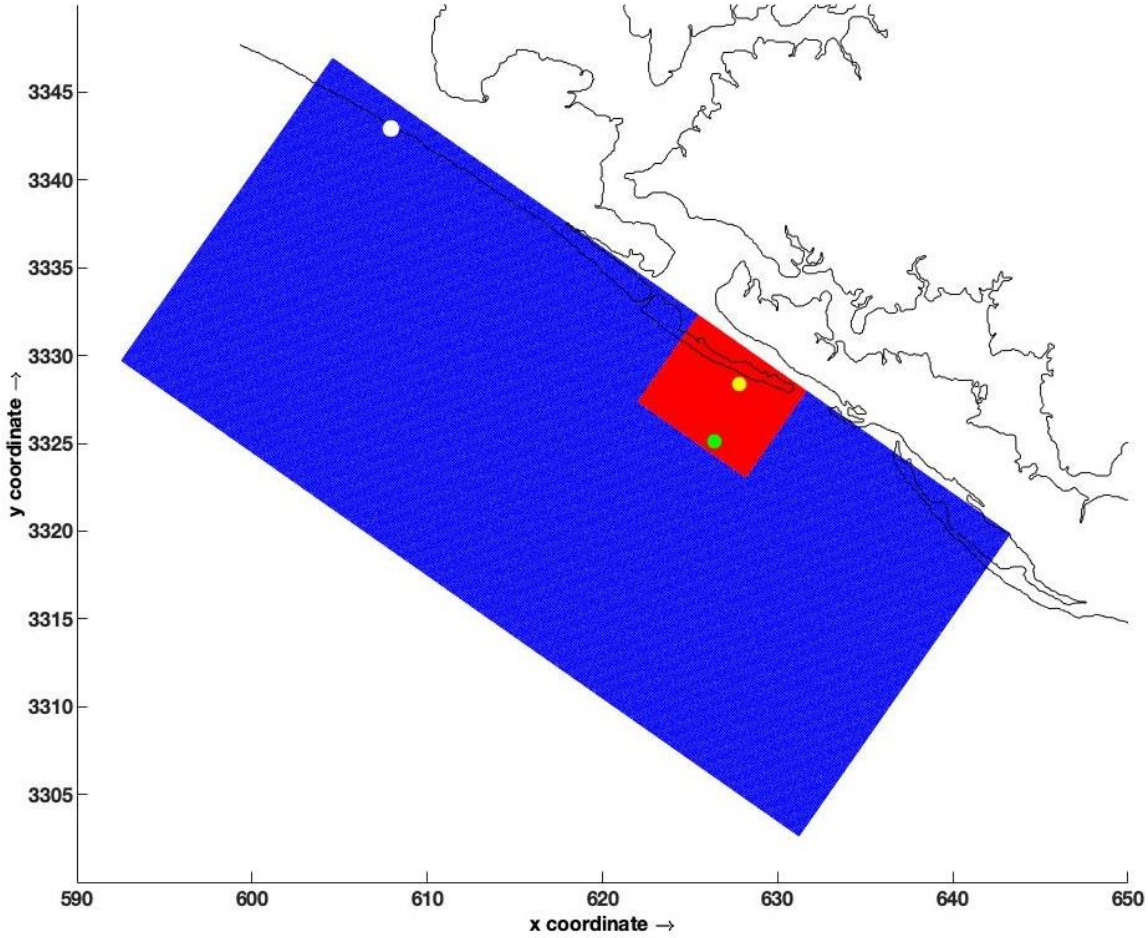

The flow outer and flow inner grids are represented in blue and red, respectively. The white dot indicates the location of the Panama City Beach tide station. The yellow and light green dots denote the location of the shallow and deep quadpods, respectively.

Figure 9. Flow computational domain.

2. Wave Grids

The wave domain covers a broader area than that of the area of interest (Figure 10) to avoid boundary effect and allow the use of buoy 42039 data available from the National

Data Buoy Center (NDBC). Considering the computational cost, four grids with different grid cell sizes were nested as a way to create a region with finer resolution.

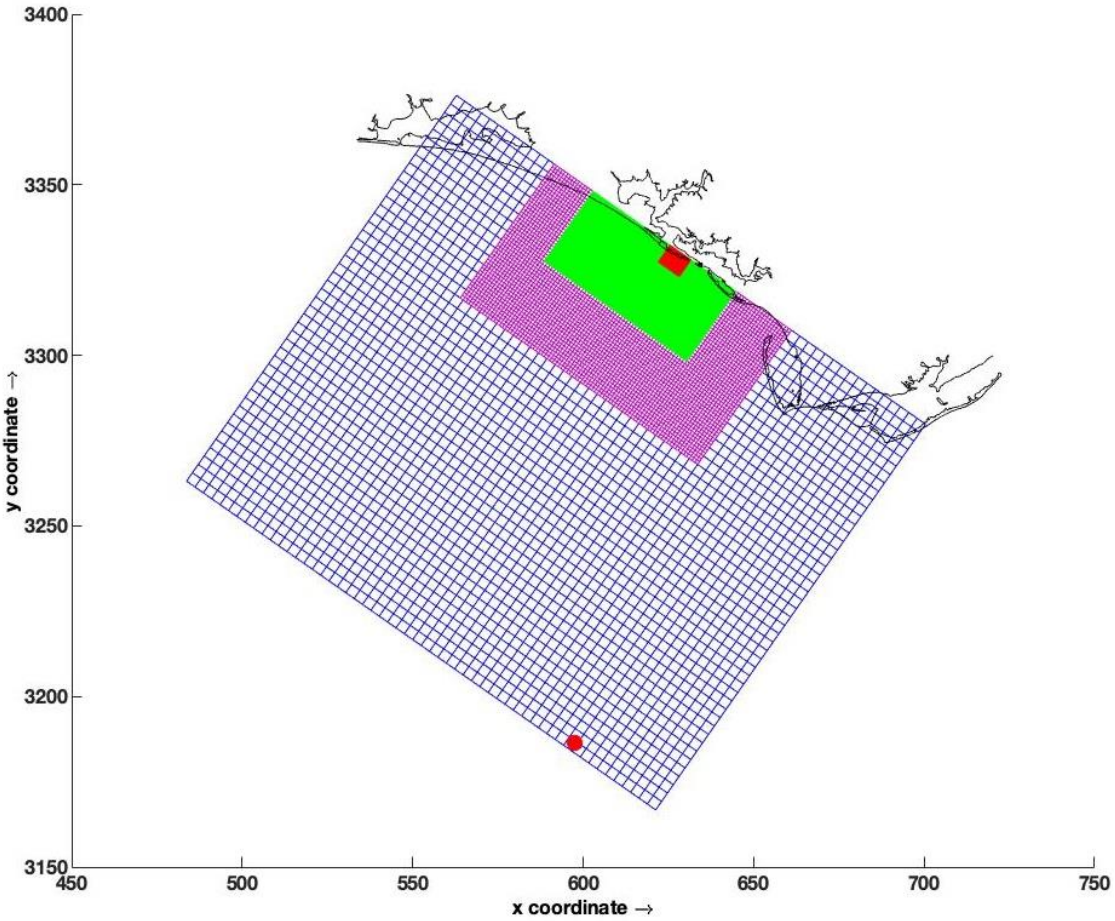

The wave outer, wave middle 1, wave middle 2, and wave inner grids are represented in dark blue, magenta, light green, and red, respectively. The red dot indicates the buoy 42039 location.

Figure 10. Wave computational domain.

All four grids are rectangular with squared cells and distinct resolution as described in Table 2. The wave inner grid resolution is 50 meters.

Table 2. Wave grids details.

Grid Name	Grid Size (km)	M	N	Cell Size (km)
Wave outer	168x138	56	46	3x3
Wave middle 1	85x48	85	48	1x1
Wave middle 2	51x25	204	100	0.25x0.25
Wave inner	8.5x6.5	170	130	0.05x0.05

M and N signify number of cells in longshore and cross-shore directions, respectively.

D. BATHYMETRIC DATA

The bathymetric data (Figure 11) used was the Northern Gulf Coast Digital Elevation Model from the National Oceanic and Atmospheric Administration/National Geophysical Data Center (NOAA/NGDC 2010). The resolution of this data set varies between 1/3 arc-second and 1 arc-second (around 10 and 30 meters).

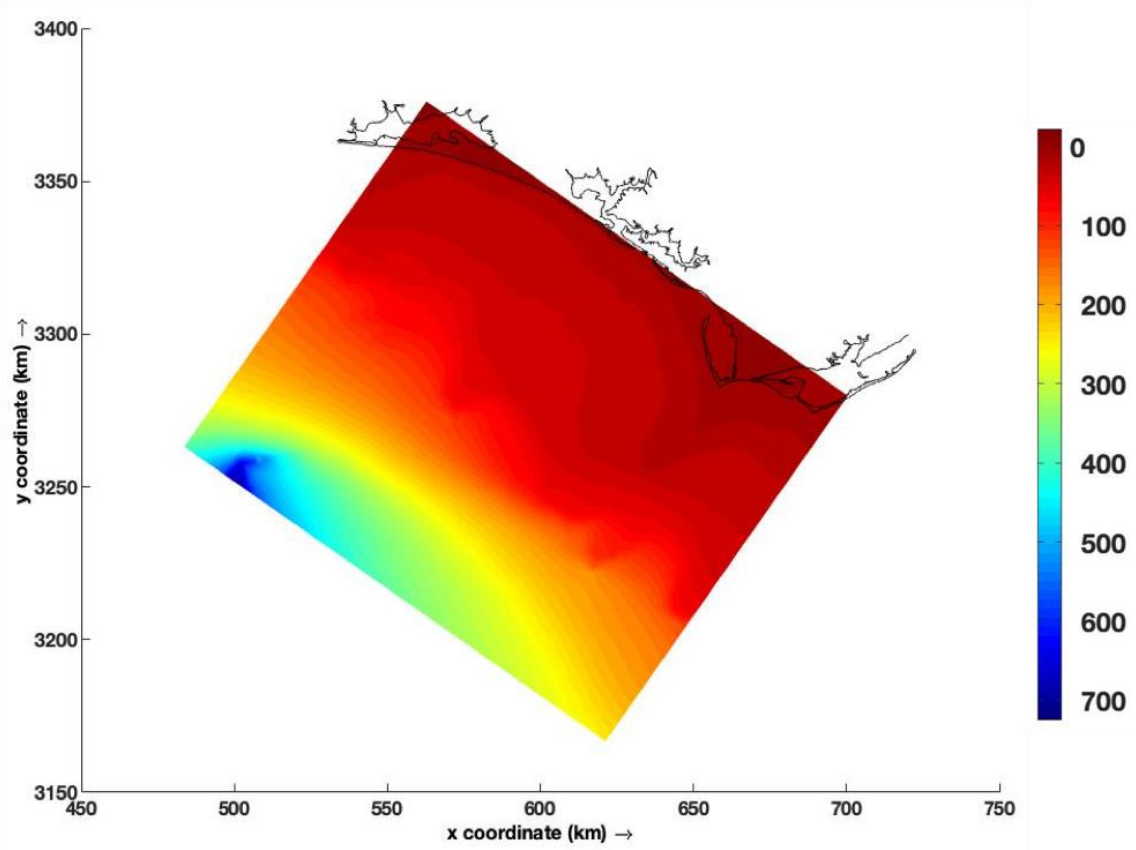

Figure 11. Bathymetry. Adapted from NOAA/NGDC (2010).

E. WIND DATA

The wind input files were set up with ERA5 Reanalysis data from the European Centre for Medium-Range Weather Forecasts (ECMWF), with 0.25° (around 28 km) resolution (ECMWF, 2019).

F. BOUNDARY CONDITIONS

1. Flow Boundary Conditions

The Global Inverse Tide Model TPXO 8.0, included in the DDB, was used to create the boundary conditions for the Delft3D-Flow module. For the longshore boundary, the water level with astronomic forcing was imposed. Conversely, for both cross-shore open boundaries, the Neumann boundary conditions were set to zero. Table 3 shows that the major tidal constituents are the diurnal constituents K1, O1, and P1.

Table 3. Tidal constituents at longshore boundary

Constituents	Amplitude (m)	Phase (deg)	Constituents	Amplitude (m)	Phase (deg)
K1	0.141	23.7	N2	0.009	110.6
O1	0.137	15.2	MF	0.007	351.9
P1	0.047	17.3	K2	0.006	90.0
Q1	0.031	357.6	MM	0.003	341.6
M2	0.029	97.8	M4	0.002	333.4
S2	0.016	90.0	MS4	0.001	315.0

2. Wave Boundary Conditions

NOAA's buoy station 42039 (NOAA/NDBC 2019) is located within the wave domain's area, but, initially, it was not used to set up the wave boundary conditions due to lack of wave direction data during the simulation period. Instead, the wave forcing boundary conditions was set up using data from the NOAA Wavewatch III Gulf of Mexico and Northwest Atlantic model results. This data set has 4-minute resolution, which is approximately 7.5 km (NOAA/NCEP 2019).

The Wavewatch III output of three specific points (Figure 12) were interpolated along their respective boundaries using parameters such as significant wave height, wave period, wave directions, and directional spreading. Later, the significant wave height and wave period data from buoy 42039 were used to improve boundary condition setup, which is better described in Chapter IV subsection A.2.

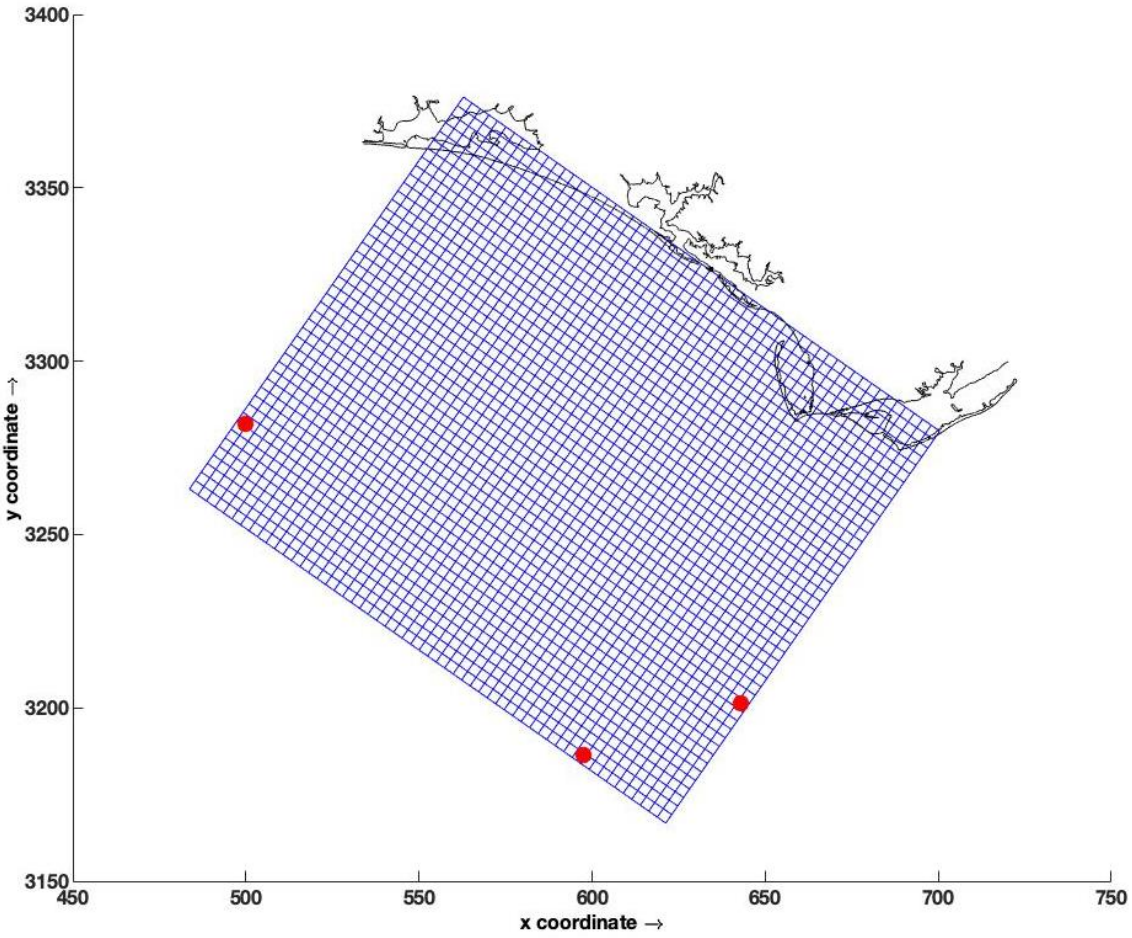

The red dots indicate the location of the three Wavewatch III output points used to set up the boundary conditions. The offshore point is the closest Wavewatch III grid point to buoy 42039.

Figure 12. Wave boundary conditions.

G. PARAMETER SETTINGS

1. Delft3d-Flow Parameter Settings

Based on the Courant-Friedrichs–Lewy number, the time step was chosen. The Courant-Friedrichs–Lewy number should not be higher than ten (Deltares 2019a) and can be computed as

$$CFL = \frac{\Delta t \sqrt{gH}}{\{\Delta x, \Delta y\}} \tag{21}$$

assuming that Δt is the time step, g denotes the acceleration of gravity, H corresponds to the total water depth, and $\{\Delta x, \Delta y\}$ is the term that expresses the grid cell size in each direction.

The bottom friction was computed from the Chézy formulation, considering a constant bottom roughness. Table 4 lists the main parameters used in the flow module.

Table 4. Main numerical parameters applied in the flow module.

Parameter	Definition	Value
Δt	time step (min)	0.1
Rhow	water density (kg/m^3)	1025
Rhoa	air density (kg/m^3)	1.15
Ccofu, Ccofv	uniform bottom roughness (m$^{1/2}$/s)	75
Vicouv	horizontal eddy viscosity (m^2/s)	0.5
Dicouv	horizontal eddy diffusivity (m^2/s)	50

2. Delft3d-Wave Parameter Settings

The wave computational mode was set as stationary and the coupling time between the flow and wave modules was set to 60 minutes. Table 5 compiles the primary wave module parameters.

The JONSWAP model from Hasselmann et al. (1973) is used to calculate the bottom friction component of wave dissipation with constant bottom friction. Also, the

model from Battjes and Jassen (1978) simulates the depth-induced breaking with α and γ as specified in Table 5.

Table 5. Main numerical parameters applied in the wave module.

Parameter	Definition	Value
BedFriction	model for bottom friction	JONSWAP
BedFricCoef	bottom friction coefficient (m^2/s^{-3})	0.038
-	depth-induced breaking model	B&J*
BreakAlpha	calibration coefficient in B&J*	1
BreakGamma	wave height to water depth ratio in B&J*	0.73

* B&J denotes Battjes and Janssen (1978)

3. Delft3d-MOR Parameter Settings

The initial bed of sediment was set to five meters for all domains. The spin-up interval was established to prevent any influence of a possible initial hydrodynamic instability on the bottom change calculation, which starts only after the spin-up interval. Table 6 lists the most significant parameters of the morphology module.

Table 6. Main numerical parameters applied in the morphology module.

Parameter	Definition	Value
MorFac	morphological scale factor	1
MorStt	spin-up interval (min)	720
SedThr	minimum water depth for sediment computations (m)	0.1
SedTyp	sediment type	sand
RhoSol	sediment-specific density (kg/m^3)	2650
SedDia	median sediment diameter - D50 (mm)	125
CDryB	dry bed density (kg/m^3)	1600

H. SUMMARY

The objective of this chapter is to present the model setup. DDB was used to create the grids and the tide-forcing boundary conditions for the coupled wave and two-dimensional flow model, including sediment transport and bottom change. Four nested grids compose the wave model, while two nested grids constitute the flow model. Wave

boundary conditions were set up including Wavewatch III output and NOAA buoy 42039 measurements. Moreover, wind data and bathymetric data from ECMWF and NOAA/NGDC, respectively, were incorporated as input data to the coupled model. The parameter settings for the flow, wave, and morphology modules are compiled in Table 4, Table 5, and Table 6, respectively.

THIS PAGE INTENTIONALLY LEFT BLANK

IV. MODEL CALIBRATION

The calibration was directed to adjust the parameters and allow a better agreement between the model output and measurements. To calibrate the model, water level, waves, and currents from the model results were compared with observations. A graphical comparison was performed to qualitatively evaluate the level of agreement between the model output and observations. Additionally, the performance of the model was quantified in terms of the parameter skill, relative mean absolute error (RMAE), root-mean-squared error (RMSE), and bias.

The parameter skill from Wilmott (1981) reveals the level of the model's accuracy in estimating the observed variable and can be calculated by:

$$Skill = 1 - \frac{\sum \left| X_{\mathrm{mod}} - X_{obs} \right|^2}{\sum \left(\left| X_{\mathrm{mod}} - \overline{X_{obs}} \right| + \left| X_{obs} - \overline{X_{obs}} \right| \right)^2} \tag{22}$$

where X is the variable of interest (e.g., water level or significant wave height), $\overline{X}$ is the time mean, the subscript mod denotes model output, and the subscript obs signifies observations. A perfect agreement between model output and observations results in a skill equal to one. In contrast, a skill equal to zero denotes complete disagreement.

Van Rijn et al. (2003) recommend applying the RMAE as a statistical criterion to evaluate the model's accuracy. They suggest that RMAE is more robust than RMSE because RMAE is less influenced by outliers. It is inconvenient that RMAE results in a significant error when the mean is close to zero; thus, it is not proper to evaluate tides, for example, but it is used here to evaluate waves and currents. The RMAE can be computed by:

$$RMAE = \left\langle \left| X_{\mathrm{mod}} - X_{obs} \right| - \Delta X_{obs} \right\rangle \Big/ \left\langle X_{obs} \right\rangle \tag{23}$$

where ΔX_{obs} denotes the measurement uncertainty and $\langle ... \rangle$ signifies time mean. Table 7 presents the model performance's qualification according to Van Rijn et al. (2003), based on the RMAE.

Table 7. Qualification of error ranges of process parameters for wave height and current speed. Adapted from Van Rijn et al. (2013).

Qualification	Wave height; RMAE	Current Speed; RMAE
Excellent	<0.05	<0.1
Good	0.05–0.1	0.1–0.3
Reasonable/Fair	0.1–0.2	0.3–0.5
Poor	0.2–0.3	0.5–0.7
Bad	>0.3	>0.7

The bias can be computed using the equation

$$Bias = \frac{1}{N}\sum\left(X_{\mathrm{mod}} - X_{obs}\right) \tag{24}$$

in which N is the number of points.

The root-mean-squared can be calculated using the equation

$$RMSE = \sqrt{\frac{1}{N}\sum\left(X_{\mathrm{mod}} - X_{obs}\right)^2}\ . \tag{25}$$

Table 8 condenses the statistical guidelines proposed by Williams and Esteves (2017) to determine the minimum performance of a model based on RMSE and bias.

Table 8. Minimum level of performance of a model. Adapted from Williams and Esteves (2017).

Model Predictions	RMSE	Bias
Water Level	No bigger than 0.1m	No bigger than 0.1m
Current Speed	Within <0.05m/s is very good, <0.1m/s is good, <0.2m/s is moderate, and 0.3m/s is poor.	No bigger than 0.15m/s

Measurements between April 21 and 27 present a significant variation in water level, waves, and currents. For this reason, this period was selected for calibration. During this process, the parameters were adjusted separately. While one was fine-tuned, the others remained constant.

A. WATER LEVEL CALIBRATION

Typically, the water level is calibrated with adjustments in the boundary conditions. The model TPXO 8.0 was used to create the flow boundary conditions as mentioned in Chapter III Subsection F. The predicted water level was compared with observed data from the Panama City Beach tide station obtained online through the DDB. Figure 13 shows significant agreement and a minimal difference in amplitude and phase between predicted and measured tide. Due to this performance, no adjustment in boundary conditions was required to calibrate the water level. The skill at the Panama City Beach tide station during the period considered for calibration is 0.976, which demonstrates that the model is quite accurate in simulating water level, as is reflected in the graph comparison (Figure 13). The computed bias is 0.028 m and RMSE is 0.033 m, which is within the range established in Table 8.

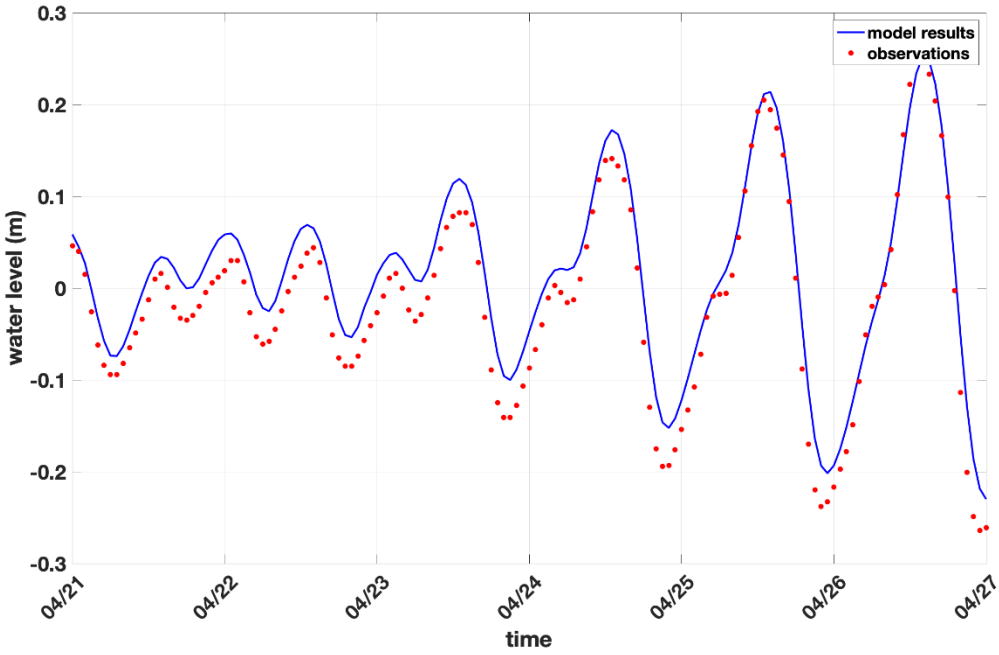

Figure 13. Water level calibration: comparison between model results and observation.

B. WAVE CALIBRATION

During the calibration process, the TREX13 measurements from both deep and shallow quadpod locations were compared with the model results. The first adjustment made in the wave model was to use the information from NOAA's buoy station 42039 to improve the boundary conditions. Initially, as described in Chapter III subsection F.2, only Wavewatch III output was used to set up the boundaries due to the lack of wave direction in the buoy's dataset. A comparison between the Wavewatch III output and the buoy's observations showed that significant wave height was underestimated, however. Thus, the bias for the entire simulation period was computed, and a correction was applied to the boundary conditions.

Table 9 presents the statistics for the wave boundary conditions adjustment considering the boundary conditions set with only Wavewatch III (BC 1) and the boundary conditions set using Wavewatch III and buoy data (BC 2). At the shallow quadpod's location, BC 1 has better results than BC 2 in all statistics, except for a slight larger bias. Moreover, BC 1's performance is considered "good" according to the RMAE criteria (Table 7), while BC 2's is classified as "fair." Unlike the shallow quadpod, the indicators were less conclusive at the deep quadpod's location, showing an equivalence between both boundary conditions options. At the deep quadpod's location, both boundary condition sets are classified as "fair" according to the RMAE criteria. BC 1 has better RMAE. BC 2 has the slightly higher skill and smaller bias. Even so, BC 1 was adopted as more appropriate in this study. The improvement attempted by calculating the bias using the available buoy data was considered ineffective.

Table 9. Statistics for the wave boundary conditions adjustment.

	Shallow Quadpod – Hs			**Deep Quadpod – Hs**		
Statistics	**BC 1**	**BC 2**	**Best Result**	**BC 1**	**BC 2**	**Best Result**
Skill	0.892	0.869	BC 1	0.860	0.879	BC 2
RMAE	0.097	0.143	BC 1	0.139	0.148	BC 1
Bias	-0.023	0.010	BC 2	-0.060	-0.017	BC 2
RMSE	0.103	0.116	BC 1	0.137	0.133	BC 2
Qualification	good	fair	BC 1	fair	fair	Equal

H_s denotes significant wave height, BC 1 is boundary conditions set with only Wavewatch III output, and BC 2 is boundary conditions set using Wavewatch III output and buoy data. The qualification follows the Van Rijn et al. (2003) criteria, as described in Table 7.

Two different JONSWAP bottom friction coefficients were tested: 0.038 m^2/s^3 and 0.067 m^2/s^3. Table 10 displays the statistics for this parameter. At the shallow quadpod's location, the coefficient equal to 0.067 m^2/s^3 presented better results in all statistics. At the deep quadpod's location, the skill is quite similar and RMSE is the same. The coefficient equal to 0.038 m^2/s^3 has a smaller bias and slightly larger RMAE. Considering the superior performance at the shallow quadpod's location, the bottom friction coefficient was chosen as 0.067 m^2/s^3.

Table 10. Statistics for the calibration of JONSWAP bottom friction coefficient.

	Shallow Quadpod – H_s Bottom friction coefficient (m^2/s^3)			**Deep Quadpod – H_s Bottom friction coefficient (m^2/s^3)**		
Statistics	0.038	0.067	Best Result	0.038	0.067	Best Result
Skill	0.870	0.875	0.067	0.879	0.875	0.038
RMAE	0.143	0.127	0.067	0.148	0.144	0.067
Bias	0.010	-0.003	0.067	-0.017	-0.030	0.038
RMSE	0.116	0.112	0.067	0.133	0.133	equal
Qualification	fair	fair	equal	fair	fair	equal

H_s denotes significant wave height. The qualification follows the Van Rijn et al. (2003) criteria as described in Table 7.

The wave height to water depth ratio (γ) in depth-induced breaking model from Battjes and Janssen (1978) was also tested for values from 0.55 to 0.73. The default value $(\gamma = 0.73)$ presented the best agreement with observations. The comparison between the wave measurements and the model results for the calibration period is presented in Figure 14. This comparison shows the significant wave heights (H_s) for locations of both the deep and the shallow quadpod.

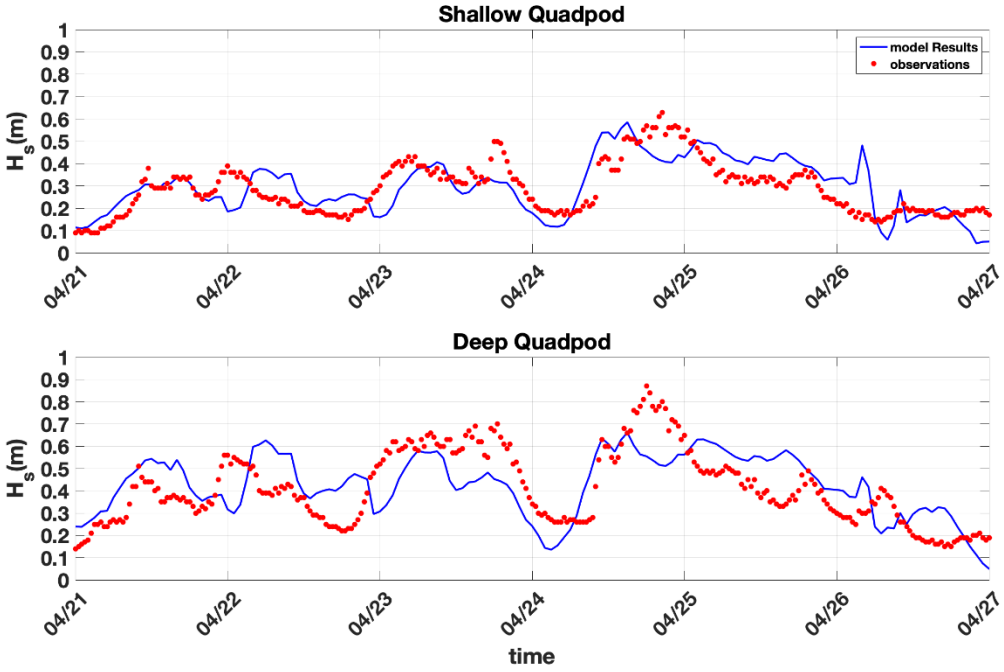

This figure presents the calibration results for the model using the parameters listed in Table 5.

Figure 14. Wave calibration: comparison between model results and observations.

C. CURRENT CALIBRATION

The flow velocities were adjusted by calibrating the Chézy friction coefficient. The model was tested for values of 65, 70, and 75 $m^{1/2}/s$, as presented in Table 11.

Table 11. Statistics for the calibration of Chézy friction coefficient.

	Chézy friction coef. ($m^{1/2}/s$)	**Skill**	**RMAE**	**Bias**	**RMSE**
Shallow Quadpod	75	0.556	0.242	-0.049	0.070
	70	0.550	0.250	-0.051	0.071
	65	0.545	0.260	-0.053	0.073
	Best Result	75	75	75	75
Deep Quadpod	75	0.363	0.199	0.003	0.053
	70	0.399	0.263	0.012	0.056
	65	0.366	0.192	0.002	0.052
	Best Result	70	65	65	65

The comparison displayed in Table 11 indicates that the model is not so sensitive to Chézy friction coefficient since results are similar. For all cases tested, the qualification was considered "good" for both criteria specified in Table 7 and Table 8. At the shallow quadpod's location, the 75 $m^{1/2}/s$ friction coefficient has superior results in all statistics. At the deep quadpod's location, the 65 $m^{1/2}/s$ friction coefficient has better results, although the performance of 75 $m^{1/2}/s$ is similar. Thus, the friction coefficient was chosen as 75 $m^{1/2}/s$. Figure 15 shows the comparison between the model results and observations during the calibration period for both quadpods.

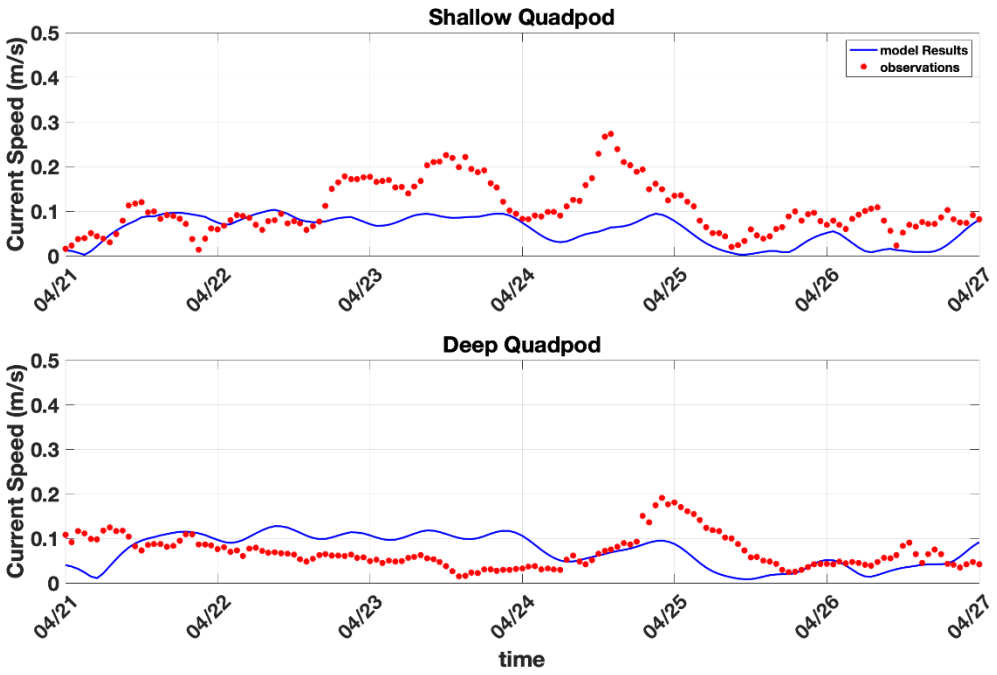

This figure presents the calibration results for the model using the parameters listed in Table 5.

Figure 15. Current calibration: comparison between model results and observations.

D. SUMMARY

Calibration was conducted to adjust the model's parameters and to improve the model capability. Statistics were computed and graphical comparisons were made to measure the performance of the model. The model's performance in simulating water level

presented satisfactory results for the calibration period and no adjustment was necessary. Waves were calibrated by fine-tuning the JONSWAP bottom friction coefficients and currents by adjusting the Chézy coefficient. During the calibration period, the performance in simulating waves and currents was considered “good” according to a qualification framework adapted from Van Rijn et al. (2003).

V. RESULTS

This chapter presents the model results for water level, waves, currents, and morphological changes during the period from April 21 to May 13, 2013.

A. HYDRODYNAMICS

1. Water Level

The model demonstrated excellent performance in simulating water level (Figure 16). The skill at the Panama City Beach tide station was calculated as 0.987, the bias as 0.014 m, and the RMSE as 0.031 m. Figure 16 shows a substantial agreement between model output and observations.

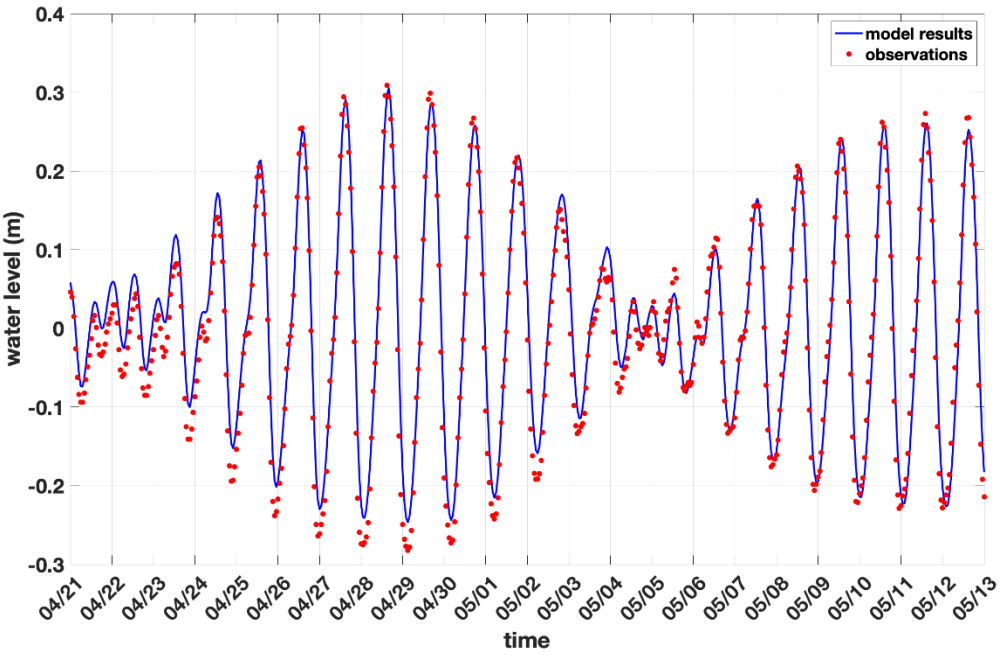

Figure 16. Water level results: comparison between model results and observation.

2. Waves

The significant wave height (H_s) and mean direction (θ) were well represented most of the time by the model in both shallow and deep quadpod locations. The model was able to represent the variation pattern of the wave peak period (T_p), but it underestimated the values along almost the whole simulation, as illustrated in Figure 17 and Figure 18. At the shallow quadpod's location, the skill was calculated as 0.896, the bias as -0.031 m, the RMAE as 0.8, and the RMSE as 0.166 m for significant wave height. At the deep quadpod's location, the skill was computed as 0.888, the bias as -0.004 m, RMAE as 0.072, and the RMSE as 0.2 m for significant wave height. The model performance is "good" considering the RMAE criteria (Table 7) for both shallow and deep quadpods.

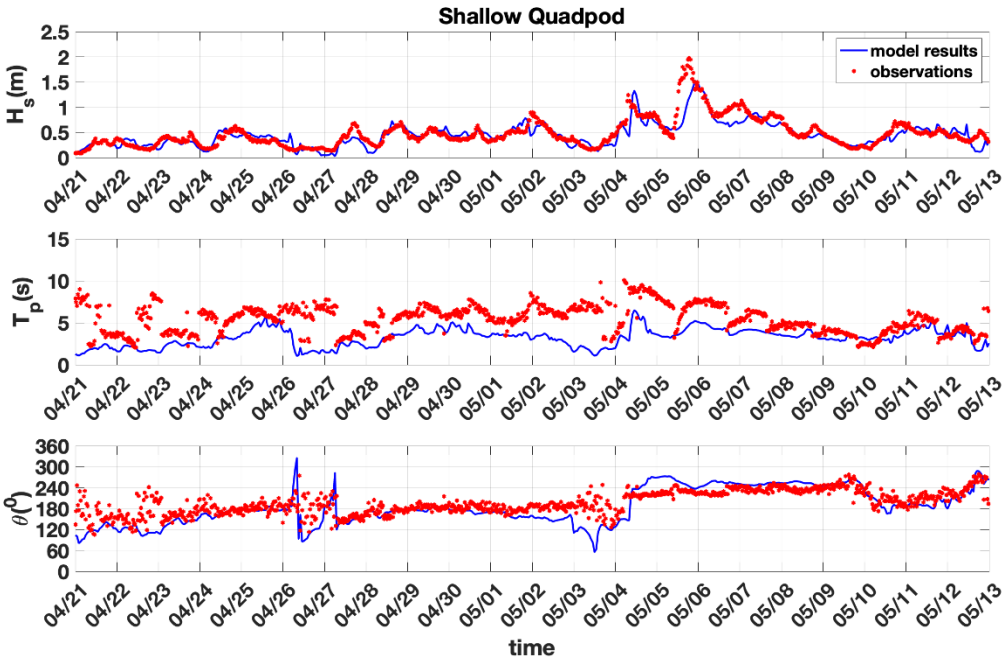

Figure 17. Model output for waves at the shallow quadpod's location.

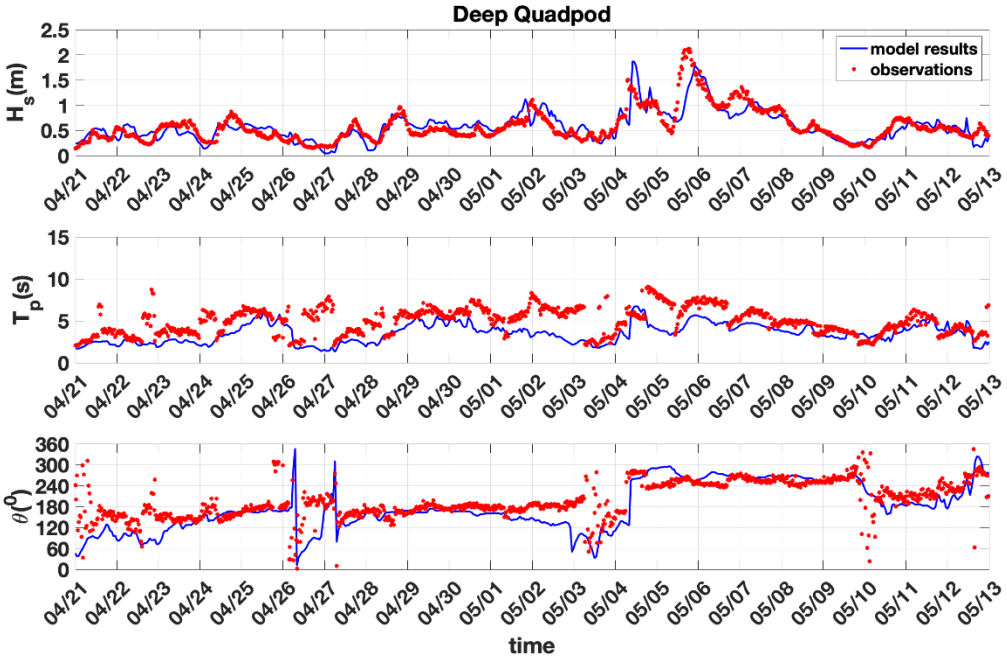

Figure 18. Model output for waves at the deep quadpod's location.

3. Currents

Especially at the shallow quadpod's location, the model was able to adequately represent the variation pattern of the current speed, but it had difficulties in describing the intensity of the current speed accurately, as shown in Figure 19 and Figure 20. At the shallow quadpod's location, the skill was computed as 0.479, the bias as -0.047 m, RMAE as 0.497, and the RMSE as 0.078 m. At the deep quadpod's location, the skill was calculated as 0.508, the bias as -0.019 m, the RMAE as 0.454, and the RMSE as 0.077 m. The model performance is reasonable considering the RMAE criteria (Table 7) for both shallow and deep quadpods.

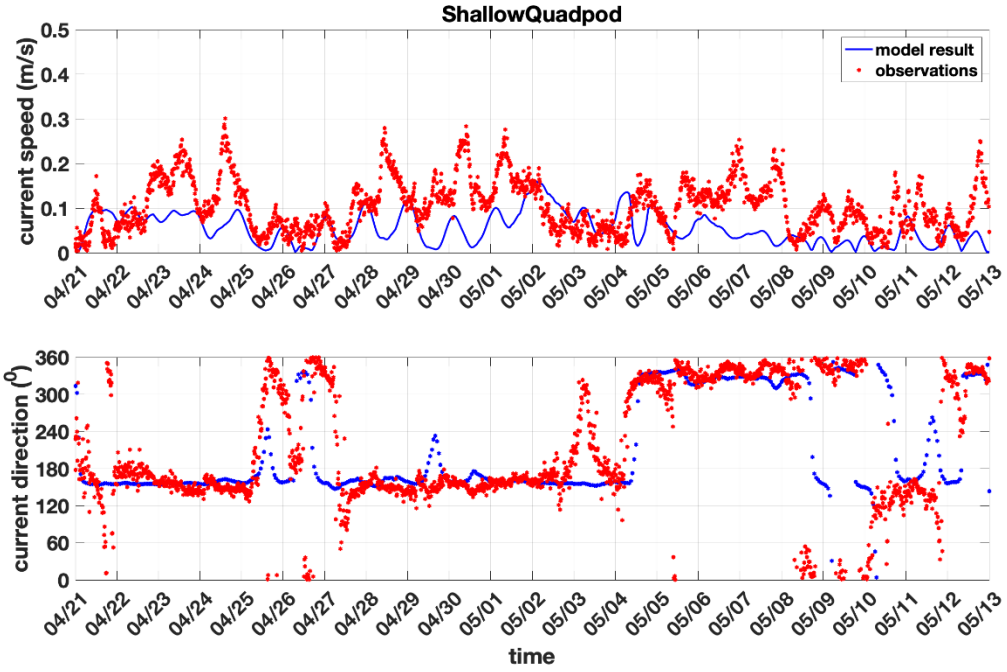

Figure 19. Model output for currents at the shallow quadpod's location.

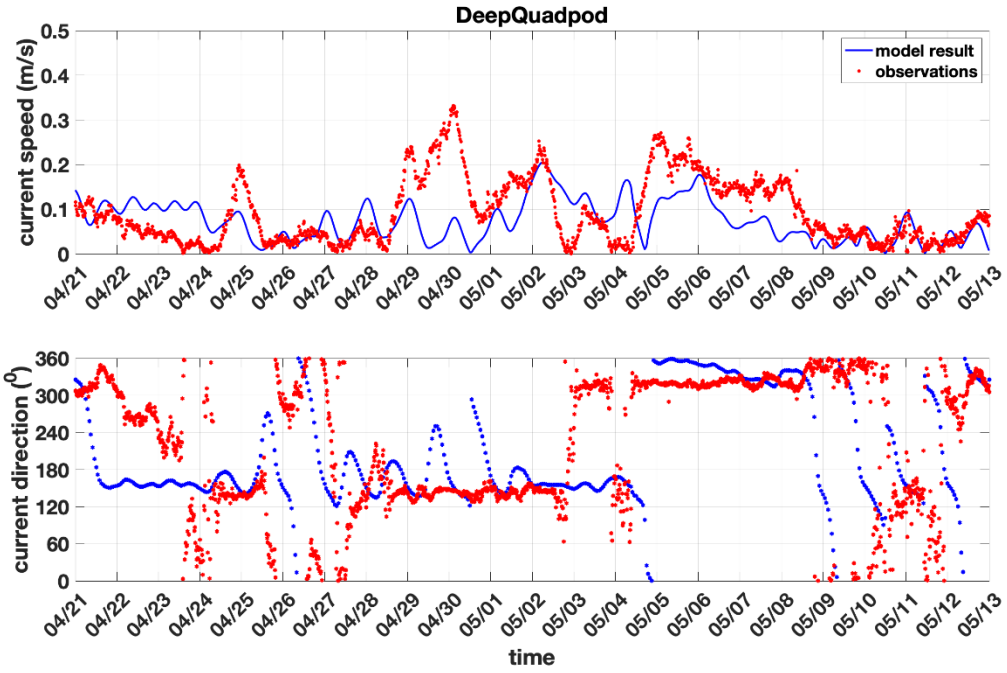

Figure 20. Model output for currents at the deep quadpod's location.

B. MORPHOLOGICAL CHANGES

According to Calantoni (2014), no bottom variations were measured at the deep quadpod's location during the storm event that occurred May 5–6 during the TREX13 experiment. Significative modifications in the seabed happened at only the shallow quadpod's location. Thus, the focus of this section is the model output at only the shallow quadpod's location. Figure 21 presents the observations and the model output on sediment accretion at the shallow quadpod. Measurements show a deposit of 0.15 m of sand after the storm. Considering that observations have a high spatial and temporal resolution, the model did adequately represent the quick increase of sediment and also the amount of deposited sediment at the end of the period. The graph also shows the sensitivity of the model regarding grain size. Considering that more than 79% of the particles collected during the TREX13 experiment are classified as fine sand (Calantoni 2014), the model was tested for different particle size D_{50}: 125μm, 150μm, and 200μm. As expected, the smallest grain size (D_{50}=125μm) gave the most significant accretion of sand.

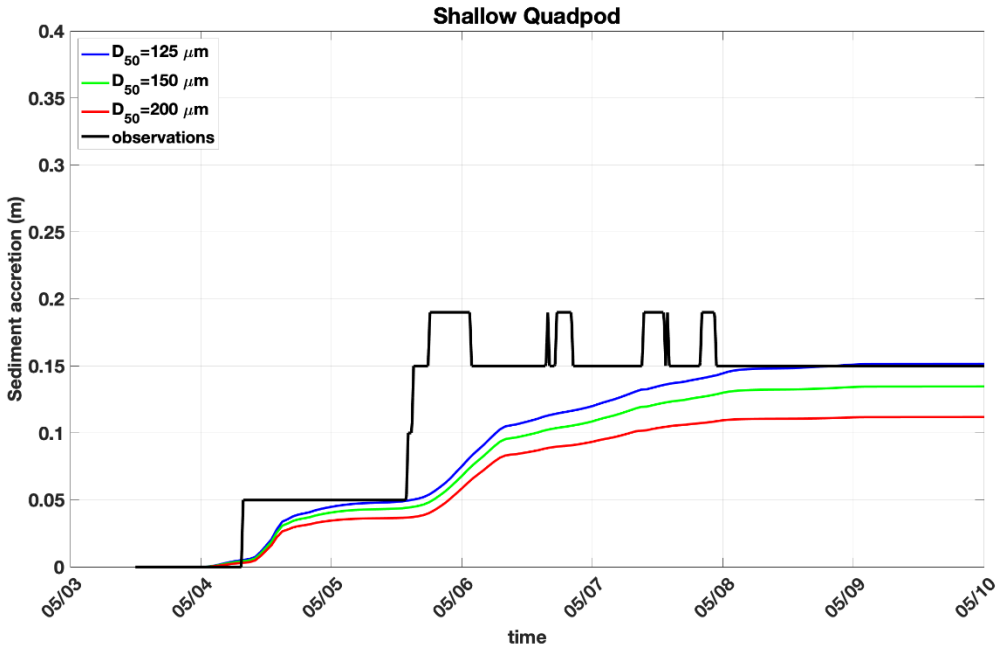

The black line indicates the observed sediment accretion estimated from maximum backscatter intensity. The blue, green, and red lines represent the model output for different particle size.

Figure 21. Sediment accretion at shallow quadpod's location. Observation and model results for different grain sizes.

Figure 22 shows the model's simulation of sediment deposit on May 8. The model predicts 0.15 m of sediment accretion at the shallow quadpod's location (zone in green) and no sediment accretion (blue) at the deep quadpod's location. Both predictions agree with observations.

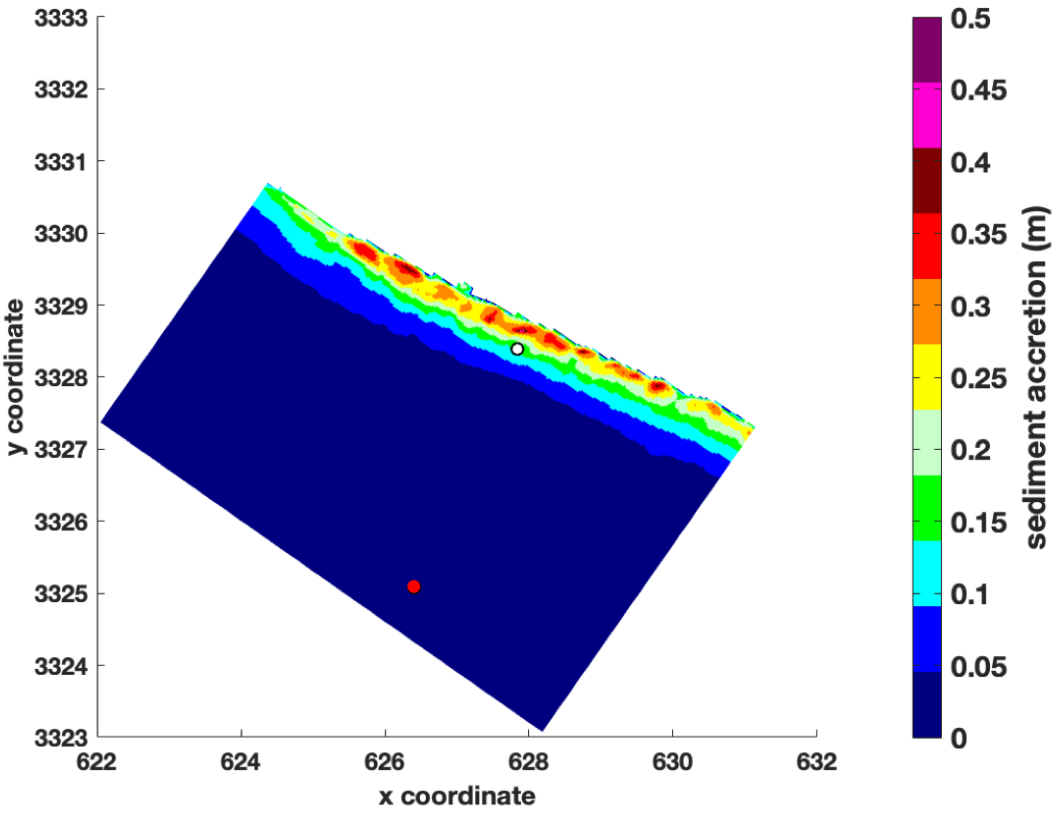

This image is the model output for sediment accretion on May 8 at 08Z. The white and red dots show the locations of the shallow and deep quadpods, respectively. At the shallow quadpod's location, the model indicates about 0.15 m of sediment accretion. At the deep quadpod's location, the model simulation indicates no accretion of sediment.

Figure 22. Sediment accretion after the storm event.

The model's capacity in simulating morphological changes is quantified by computing the Brier Skill Score (BSS), as suggested by Van Rijn et al. (2003):

$$BSS = 1 - \left[\left\langle \left(\left| z_{b,c} - z_{b,m} \right| - \Delta z_{b,m} \right)^2 \right\rangle \Big/ \left\langle \left(z_{b,0} - z_{b,m} \right)^2 \right\rangle \right] \tag{26}$$

in which $z_{b,c}$ denotes the computed bed level, $z_{b,m}$ is the measured bed level, $z_{b,0}$ signifies the initial bed level, and $\Delta z_{b,m}$ is the uncertainty of the measured bed level. Table 12 presents the qualification of the model's performance according to the BSS suggested by Van Rijn et al. (2003). Table 13 presents the BSS for the simulations with different particle sizes.

Table 12. Qualification of error ranges of process parameters for morphology. Adapted from Van Rijn et al. (2013).

Qualification	**Morphology; BSS**
Excellent	1.0–0.8
Good	0.8–0.6
Reasonable/fair	0.6–0.3
Poor	0.3–0
Bad	<0

Table 13. Statistics and qualification for the morphological changes.

D_{50}	**BSS**	**Qualification**
125μm	0.852	Excellent
150μm	0.812	Excellent
200μm	0.747	Good

Qualification follows the Van Rijn et al. (2003) criteria, as described in Table 12.

C. LIMITATIONS

The depth-averaged modeling assumes that currents follow a logarithmic vertical distribution. In real-word situations, however, currents might have a different vertical profile, reducing the accuracy of the model output.

The bathymetric data used in this study comes from a survey dating from 2010, three years before the TREX13 experiment. The bathymetry of the beginning and end of the experiment period would be very useful to calibrate and evaluate the model performance more precisely.

The wind data used as input for the model has a resolution of 28 km, which may not be the most appropriate one. It can impact the hydrodynamic results, mainly in waves and currents.

Wave boundary conditions were set using the output from the Wavewatch III model. There is a NOAA buoy in the area of interest, but no data from this buoy is available for the experiment period. The use of Wavewatch III rather than observations to set up the wave boundary conditions may impact the model accuracy.

VI. CONCLUSIONS

Essential processes capable of causing the munitions' movement on the seabed, such as waves, currents, and sediment transport, were measured between April and May 2013, on the coast of Panama City, Florida. During a storm event May 5–6, observers measured the movement and rapid burial of surrogate munitions under 0.15 meters of sand, which delivers a challenging record for a modeling study.

A nearshore process model using the Delft3D system was set up to simulate flow, waves, and morphological responses to the storm event. Four grids were nested to create the wave domain and two grids to compose the flow domain. The output from the Wavewatch III model was used to set the wave boundary conditions. Regarding the flow boundary conditions, the longshore boundary was set as water level, and both lateral boundaries were set as Neumann boundary condition.

A calibration process was conducted to achieve a better agreement between observations and model results. In this procedure, parameters such as the JONSWAP bottom friction coefficient, wave height to water depth ratio (γ), and Chézy coefficient were tested and adjusted. The model performance was evaluated by graphical comparison and by computing the parameter skill, Relative Mean Absolute Error (RMAE), Root-Mean-Squared Error (RMSE), and bias.

A simulation of April 21–May 13 was conducted and the model output was compared with observations. The model demonstrated excellent performance in representing the water level with a skill parameter equal to 0.987, bias equal to 0.014 m, and RMSE equal to 0.031 m. The model's ability to simulate waves is considered "good" according to the criteria established by Van Rijn at el. (2003). The results for currents were qualified as "reasonable," although the model encounters difficulties in accurately estimating the current speed in some periods. The model accurately captured the sand accretion that occurred during the storm event and achieved a BSS of 0.852, which is considered "excellent," according to Table 12.

Even with some limitations, such as the depth-averaged modeling approach and usage of an out-of-date bathymetry, the model demonstrated a satisfactory capability to simulate the hydrodynamic and the bottom change observed during the storm event.

LIST OF REFERENCES

Battjes, J. A., and J. P. F. M. Janssen, 1978: Energy loss and set-up due to breaking random waves. Proceedings of the 16th International Conference on Coastal Engineering, *Am. Soc. of Civ. Eng.*, 569–587.

Booij, N., R. C. Ris, and L. H. Holthuijsen, 1999: A third-generation wave model for coastal regions: 1. Model description and validation. *J. Geophys. Res.*, **104**(C4), 7649–7666.

Bunya, S., and Coauthors, 2010: A high-resolution coupled riverine flow, tide, wind, wind wave, and storm surge model for Southern Louisiana and Mississippi. Part I: Model development and validation. *Mon. Wea. Rev*., **138**, 345–377.

Collins, W. D., and Coauthors, 2006: The formulation and atmospheric simulation of the Community Atmosphere Model Version 3 (CAM3). J. Climate, 19, 2144–2161, https://doi.org/10.1175/JCLI3760.1.

Calantoni, J., 2014: Long time series measurements of munitions mobility in wave-current boundary layer. Report SERDP Project Number 2320, U.S. Naval Research Laboratory.

Chu, P.C., and C.W. Fan, 2006: Prediction of falling cylinder through air-water-sediment columns. *ASME J. Appl. Mechanics*, **73**, 300–314.

Chu, P. C., P. Pauly, S. D. Haeger, M. Ward, 2006: Wind and tidal effects on chemical spill in St Andrew Bay system. *Coastal Environment and Water Quality*, 47–68.

Collins, J. I., 1972: Prediction of shallow-water spectra, *J. Geophys. Res*., **77**(15), 2693–2707.

Deltares, 2019a: Delft3D-Flow—Simulation of multi-dimensional hydrodynamic flows and transport phenomena, including sediments. User Manual, Delft, the Netherlands, https://content.oss.deltares.nl/delft3d/manuals/Delft3D-FLOW_User_Manual.pdf.

Deltares, 2019b: Delft3D-Wave—Simulation of short-crested waves with SWAN - User Manual, Delft, the Netherlands, https://content.oss.deltares.nl/delft3d/manuals/Delft3D-WAVE_User_Manual.pdf.

Eldeberky, Y., and J. A. Battjes, 1996: Spectral modeling of wave breaking: Application to Boussinesq equations. *J. Geophys. Res*., **101**(C1), 1253–1264.

ECMWF, 2019: ERA5 Reanalysis (0.25 Degree Latitude-Longitude Grid). Research Data Archive at the National Center for Atmospheric Research, Computational and Information Systems Laboratory, Boulder, CO, accessed July 3, 2019, https://doi.org/10.5065/BH6N-5N20.

Farrar, P. D., L. E. Borgman, L. B. Glover, R. D. Reinhard, J. Pope, A. Swain, B. A. Ebersole, 1994: Storm impact assessment for beaches at Panama City, Florida. U.S. Army Engineer Waterways Experiment Station. Report CERC-94-11, 207pp, http://citeseerx.ist.psu.edu/viewdoc/download?doi=10.1.1.371.2181&rep=rep1&type=pdf.

Google Earth. Panama City map. Accessed November 1, 2019, https://earth.google.com/web/@30.06040978,-85.68117843,-2.92770849a,22402.70954094d,35y,-1.50170942h,2.37939347t,0r.

Google Maps. Panama City map. Accessed November 1, 2019, https://www.google.com/maps/place/Panama+City,+FL/@28.2711045,-86.0464551,7.21z/data=!4m5!3m4!1s0x889381562ac66341:0xbf585ed52c4701f3!8m2!3d30.1588129!4d-85.6602058?hl=en.

Hasselmann, K., 1962: On the non-linear energy transfer in a gravity-wave spectrum: Part 1. General theory. *J. Fluid Mech.*, **12**, 481–500.

Hasselmann, K., and Coauthors, 1973: Measurements of wind wave growth and swell decay during the Joint North Sea Wave Project (JONSWAP). *Dtsch Hydrogr. Z. Suppl.*, **12**(A8), 1–95.

Hasselmann, K., 1974: On the spectral dissipation of ocean waves due to white capping. *Boundary-Layer Meteor.*, **6**(1), 107–127.

Hasselmann, S., and K. Hasselmann, 1985: Computations and parameterizations of the nonlinear energy transfer in a gravity-wave spectrum. Part I: A new method for efficient computations of the exact nonlinear transfer integral. *J. Phys. Oceanogr.*, **15**, 1369–1377.

Jenkins, S.A., D.L. Inman, M.D. Richardson, T.F. Wever, and J. Wasyl, 2007: Scour and burial mechanics of objects in the nearshore. *IEEE J. of Oceanic Engineering*, **32**, 78–90.

Komar, P. D., 1976: *Beach Processes and Sedimentation*. Prentice Hall, 429 pp.

Madsen, O., Y. Poon, and H. Graber, 1988: Spectral wave attenuation by bottom friction: theory. *Coastal Engineering Proceedings*, **1**(21), 34.

McDonald, J., R., 2009: Marine UXO surveys: logistics and operational challenges. Technical report SERDP-ESTCP, project number MM2003-24, 67, https://www.serdp-estcp.org/content/download/4457/66225/file/MM-0324%20TR.pdf.

NOAA/NCEP, 2019: Wavewatch III Gulf of Mexico and Northwest Atlantic 4 min. NOAA/National Centers for Environmental Prediction, accessed July 26, 2019, ftp://polar.ncep.noaa.gov/pub/history/waves/multi_1.

NOAA/NDBC, 2019: NOAA Meteorological/Ocean Station 42039. NOAA/National Data Buoy Center, accessed June 8, 2019, https://www.ndbc.noaa.gov.

NOAA/NGDC, 2010: Northern Gulf 1 arc-second MHW Coast Digital Elevation Model. NOAA/National Geophysical Data Center, accessed May 6, 2019, https://maps.ngdc.noaa.gov/viewers/bathymetry/?layers=dem.

Phillips, N. A., 1957: A coordinate system having some special advantages for numerical forecasting. *J. Meteor.*, **14**, 184–185.

Plant, N. G., J. W. Long, P. S. Dalyander, D. M. Thompson, E. A. Raabe, 2013: Application of a hydrodynamic and sediment transport model for guidance of response efforts related to the Deepwater Horizon oil spill in the northern Gulf of Mexico along the coast of Alabama and Florida. U.S. Geological Survey. Report number 2012–1234, http://pubs.usgs.gov/of/2012/1234/.

Roelvink, D., and A. Reniers, 2012: *A guide to modeling coastal morphology*. World Science Publishing Co. Pte. Ltd, 274 pp.

SERDP-ESTCP, 2010. Munitions in the Underwater Environment: State of the Science and Knowledge Gaps. White paper, 12pp, https://www.serdp-estcp.org/Featured-Initiatives/Munitions-Response-Initiatives/Munitions-in-the-Underwater-Environment/White-Paper-Munitions-in-the-Underwater-Environment

Shields, A. 1936: Application of similarity principles and turbulence research to bedload movement. Soil Conservation Service Laboratory, California Institute of Technology. Pasadena, California.

Taiani, L., L. Benedet, L. Silveira, S. Keehn, N. Sharp, R. Bonanata, 2012: Sand borrow area design refinement to reduce morphological impacts: A case study of Panama City Beach, Florida, USA. *Coastal Engineering Proceedings*, **1**(33), sediment 103.

Van Rijn, L.C., 1993: *Principles of Sediment Transport in Rivers, Estuaries and Coastal Seas*. Aqua Publications, 715pp.

Van Rijn, L. C., 2000: General view on sand transport by currents and waves: data analysis and engineering modelling for uniform and graded sand (TRANSPOR 2000 and CROSMOR 2000 models). Delft Hydraulics. Report Z2899, 121pp, http://resolver.tudelft.nl/uuid:3239959b-8f88-4193-ae9c-ce7d8e38be59.

Van Rijn, L.C., D. Walstra, B. Grasmeijer, J. Sutherland, S. Pan, and J. Sierra, 2003: The predictability of cross-shore bed evolution of sandy beaches at the time scale of storms and seasons using process-based Profile models. *Coastal Engineering*, **47**(3), 295–327.

Van Rijn, L.C., 2014: A simple general expression for longshore transport of sand, gravel and shingle. *Coastal Engineering*, **90**, 23–39.

WAMDI Group, 1988: The WAM Model: A third generation ocean wave prediction model. *J. Phys. Oceanogr.*, **18**, 1775–1810.

Whitham, G. B., 1974: *Linear and Nonlinear Waves*. Wiley, 663 pp.

Williams, J., and L. Esteves, 2017: Guidance on Setup, Calibration, and Validation of Hydrodynamic, Wave, and Sediment Models for Shelf Seas and Estuaries. *Advances in Civil Engineering*, **2017**, 1–25.

Willmott, C.J., 1981: On the Validation of Models. *Physical Geography*, **2**, 184–194.

INITIAL DISTRIBUTION LIST

1. Defense Technical Information Center
   Ft. Belvoir, Virginia

2. Dudley Knox Library
   Naval Postgraduate School
   Monterey, California